PCCP

ROYAL SOCIETY OF CHEMISTRY

PAPER

Cite this: *Phys. Chem. Chem. Phys.*, 2023, **25**, 3986

DFT computations combined with semiempirical modeling of variations with temperature of spectroscopic and magnetic properties of Gd^{3+}-doped $PbTiO_3$†

Muhammed Acikgoz, *[a] Leila Mollabashi, [b] Shahrbano Rahimi, [b] Saeid Jalali-Asadabadi *[b] and Czesław Rudowicz [c]

The rare-earth or 3d transition metal dopants in perovskites have potential to induce interesting features, thus opening opportunities for investigations and applications. Hence, understanding some features, *i.e.*, defect structure, site of incorporation, valence state, and mechanism of charge compensation, in a wide range of temperature is crucial for their technological applications. A comprehensive understanding of the mechanism of structural changes in $PbTiO_3$ doped with trivalent rare-earths is significant for their potential applications in photonics. To unravel the structural changes, we utilize the density functional theory (DFT) to optimize structural data, which then serve as input for the semiempirical superposition model (SPM) analysis of spectroscopic and magnetic properties of Gd^{3+}-doped $PbTiO_3$. We compute the formation energies of the doped compounds with and without O-vacancy to determine the stable composition. Analysis of the Bader electron charges computed using DFT plus quantum theory of atoms in molecules enables elucidating the effects of the Gd dopant and O-vacancy on the ionic and covalent bonds and, thereby, chemical stability of the compositions. To explain and corroborate the zero-field splitting parameters (ZFSPs) measured by EMR and the lattice parameter changes obtained from XRD, we employ SPM. The optimized structures obtained from *ab initio* computations for various structural models of Gd^{3+} doped $PbTiO_3$ are utilized as input data for SPM calculations of ZFPs. This enables theoretical analysis of variations of ZFSPs from 5 to 780 K. The results were fine-tuned by matching with available experimental EMR data for Gd^{3+} probes in $PbTiO_3$ nanoparticles. Modeling has been carried out considering several possible structural models and the role of an O-vacancy around Gd^{3+} centers. The results show that the two-fold modeling approach, combining DFT and SPM, provides a reliable description of experimental data. Comparative analysis indicates that the Ti-site is less favorable for being replaced by Gd^{3+} with/without O-vacancy. This analysis confirms the plausibility of the Pb^{2+} site for Gd^{3+} dopants and sheds light on the changes of crystal structure during the phase transitions occurring in $PbTiO_3$ with decreasing temperature.

Received 7th July 2022,
Accepted 4th January 2023

DOI: 10.1039/d2cp03098e

rsc.li/pccp

1. Introduction

Lead titanate ($PbTiO_3$), being a displacive type ferroelectric material, is one of the most useful and explored crystals of the perovskite family.[1,2] The perfect physical and electromechanical properties make $PbTiO_3$ widely used as a functional ceramic, especially as a dielectric in capacitors and athin films with high refractive index for electro-optical components. Most recently, the performance enhancement and temperature dependence of the piezoelectric properties of $Pb(Mg_{1/3}Nb_{2/3})$-O_3-0.30$PbTiO_3$ single crystals by alternating current polarization were studied.[3] Moreover, doping of pure $PbTiO_3$ with some trivalent rare-earth (RE) or 3d transition metal (TM) dopant ions may induce additional interesting features, thus opening numerous opportunities for investigations and potential applications. Particularly, understanding these features and their variations in a wide range of temperature is crucial for technological applications of this compound, which depend on the defect structure, site of incorporation, valence state, and mechanism of charge compensation in oxide ferroelectrics as reviewed by Eichel.[4]

[a] *Department of Science, The State University of New York (SUNY) Maritime College, New York 10465, USA. E-mail: macikgoz@sunymaritime.edu*
[b] *Department of Physics, Faculty of Physics, University of Isfahan (UI), Hezar Jerib Avenue, Isfahan 81746-73441, Iran. E-mail: sjalali@sci.ui.ac.ir*
[c] *Faculty of Chemistry, A. Mickiewicz University (AMU), 61-614 Poznań, Poland*

† Electronic supplementary information (ESI) available. See DOI: https://doi.org/10.1039/d2cp03098e

An important aspect is the actual location of dopant ions in the host $PbTiO_3$ lattice. Lead titanate has an ABO_3 perovskite structure with space group $C_{4v}(P4mm)$.[5] Concerning Gd^{3+}:$PbTiO_3$, based on comparison of the ionic radii, it was suggested that the Gd^{3+} ions substitute at the Pb^{2+} A-sites.[5] This suggestion has been corroborated by electron magnetic resonance (EMR; alternatively called electron paramagnetic resonance: EPR) study, which determined the spin Hamiltonian (SH) parameters for Gd^{3+} ions in $PbTiO_3$.[5] However, analysis of the pulsed high-frequency EMR (HF-EMR) spectra[6] of Gd-doped $PbTiO_3$ and $PbZrO_3$ has indicated that Gd^{3+} ions may also be located at highly distorted sites. This finding likely indicates that, under high doping conditions, charge compensation may lead to the formation of closely correlated Gd^{3+}-V_{Pb}''-Gd^{3+} defects. In contrast to the accepter-type dopants, like Fe^{3+} and Cu^{2+}, the donor-type Gd^{3+} dopant is incorporated as an '*isolated*' functional center, where charge compensation by means of lead vacancies occurs in distant coordination spheres.[7] Such defects yield additional EMR lines differing from those due to Gd^{3+} ions entering substitutionally at Pb^{2+} sites with undistorted oxygen and lead neighboring shells. In the low-temperature orthorhombic phase of $PbZrO_3$, two crystallographically inequivalent Pb^{2+} sites of an equal amount are present. The contribution of Gd^{3+} inserted substitutionally at these sites has been confirmed by van Tol *et al.*[6] The authors[6] interpreted the EMR spectra using a different SH notation than that used by Eichel *et al.*[5] For an overview of the SH notations existing in the literature and inter-conversion relations the readers may consult reviews.[8–10]

The scope of this research is to (i) reconsider the available EMR data[4–7] since the findings[4–6] were based on truncated SH forms[8–10] and are somewhat disparate, (ii) provide more consistent and conclusive explanations of the observed spectroscopic and magnetic properties of Gd^{3+}:$PbTiO_3$, and (iii) model and predict variations of these properties with temperature for Gd^{3+}:$PbTiO_3$ bulk and nanopowder samples with varying compositions: $Pb_{1-y}Gd_yTiO_{3-\delta}$ and $PbTi_{1-y}Gd_yTiO_{3-\delta}$, where the stoichiometric parameter δ denotes the presence of the O-vacancy. To the best of our knowledge, no comprehensive theoretical analysis of temperature dependence of the zero-field splitting (ZFS) parameters (ZFSPs)[8–10] obtained from the SH analysis of EMR spectra for Gd^{3+}:$PbTiO_3$ has been carried out yet. The present paper attempts to fill this gap. To this end, a two-fold modeling approach is employed.

First, we utilize the density functional theory (DFT)[11,12] as implemented in the WIEN2k code[13] to perform geometry optimization of structural data. In order to find the plausible site for doping Gd the formation energies are computed with and without considering the oxygen vacancy to determine the stable doped composition. To elucidate how the Gd dopant and O-vacancy can influence the ionic and covalent bonds, the Bader electron charges (BECs) are computed using quantum theory of atoms in molecules (QTAIM),[15,16] as implemented in the CRITIC2 code.[17,18] To this end, the electron charge densities generated by DFT are used as an input for the QTAIM postprocessing computations to produce the BECs. Analysis of the computed BECs enables qualitative investigation of the effects of the Gd dopant and oxygen vacancy on the strength of the ionic and covalent bonds and thereby chemical stability of the pure compound and the doped compositions in the presence and absence of the O-vacancy.

Next, we utilize the DFT results as input for the semiempirical superposition model (SPM) analysis[19–21] (see Section I in the ESI†) to investigate variations of spectroscopic and magnetic properties of Gd^{3+}-doped $PbTiO_3$ with temperature as well as for various compositions: $Pb_{1-x}Gd_xTiO_{3-\delta}$ and $PbTi_{1-x}Gd_xTiO_{3-\delta}$. The two-fold modeling approach enables explanation of the temperature dependence of ZFSPs observed in Gd^{3+}-doped $PbTiO_3$ and consideration of possible distortions around Gd^{3+} ions.

Hence, the present results may be useful in future studies aimed at technological applications of the $PbTiO_3$ host doped with various RE and TM ions.

Additional motivation for this study stems from our current investigations aimed at rational design of molecular nanomagnets based on RE and TM ions and computational modeling of their properties.[22,23] Molecular nanomagnets comprise the single-molecule magnets (SMM), single-ion magnets (SIM), and single-chain magnets (SCM).[24–27] These systems have been extensively studied due to, among others, the phenomenon of macroscopic quantum tunneling of magnetization as well as possible applications in high-density information storage and quantum computing.[24–27] Recently several novel SMM or SCM systems with elaborate coordination geometry containing also Gd^{3+} ions have been synthesized and studied experimentally and theoretically.[28–32] Model calculations for simpler systems may provide grounds for studies of more complicated SMM, SIM or SCM systems. Importantly, the sets of model parameters determined in the present SPM analysis for Gd^{3+} in $PbTiO_3$ may be utilized for ZFSP calculations for these ions at similar sites in ABO_3 perovskites as well as SMM, SIM or SCM systems. As a follow-up to the studies,[22,23] complexes based on two exchange coupled Gd^{3+} ions surrounded by various ligands have recently been synthesized in our research group at the AMU as potential SMM.[33] The study[33] tests the suitability of combining experimental EMR data and predictions based on crystal field (CF) theory as well as modelling of ZFSPs using and SPM analysis and DFT methods, and thus prepares grounds for consideration of the spectroscopic and magnetic properties of such systems. Most recently, the incorporation of S-state lanthanide ions, like Gd^{3+}, in non-magnetic matrices, *e.g.*, $CaWO_4$, has generated considerable interest as potential candidates for a quantum hybrid system when integrated into current circuit quantum electrodynamics (QED) architectures.[34]

2. Analysis of experimental EMR data for Gd^{3+}:$PbTiO_3$

For description of EMR spectra and the energy levels of the ground spin (S) state of paramagnetic TM/RE ions exhibiting an orbital singlet ground state in crystals[35–38] we adopt the

reference SH consisting of the Zeeman electronic terms and the ZFS terms:[8–10,39,40]

$$H = H_{Ze} + H_{ZFS} = \mu_B B \cdot g \cdot S + \sum B_k^q O_k^q = \mu_B B \cdot g \cdot S + \sum f_k b_k^q O_k^q, \quad (1)$$

where g is the spectroscopic splitting factor, μ_B is the Bohr magneton, B is the applied magnetic field, S is the effective spin operator, and B_k^q and b_k^q are the ZFS parameters associated with O_k^q which is the extended Stevens operator.[41,42] The scaling factors[8–10] are f_k = 1/3, 1/60, and 1/1260 for k = 2, 4, and 6, respectively. For the Gd^{3+}($4f^7$, $^8S_{7/2}$) ion in a lattice site with tetragonal type I symmetry (D_4, C_{4v}, D_{2d}, D_{4h}), the non-zero Zeeman electronic parameters are $g_{\parallel\parallel}$ and $g_\perp$, whereas the ZFSPs b_k^q used in this study are defined in eqn (2):

$$H_{ZFS} = \frac{1}{3}b_2^0 O_2^0 + \frac{1}{60}b_4^0 O_4^0 + \frac{1}{60}b_4^4 O_4^4 + \frac{1}{1260}b_6^0 O_6^0 + \frac{1}{1260}b_6^4 O_6^4 + \frac{1}{1260}b_6^6 O_6^6 \quad (2)$$

Note that the simplest form of the ZFS terms, as in eqn (2), is obtained only in the symmetry-adapted axis system (x, y, z).[8–10,43]

To enable comparative analysis of our theoretical and experimental results, below we overview the reported EMR results on Gd^{3+} in $PbTiO_3$ in view of the reference SH notation in eqn (1) and (2). By numerical simulation of the EMR spectra Eichel *et al.*[5] determined the SH parameters for Gd^{3+}:$PbTiO_3$ as $g = 1.992 \pm 0.002$ and $|B_2^0| = 0.776(2)$ GHz at room temperature (RT) as well as only one much smaller fourth-rank ZFSP $|B_4^0| = 7.67(1)$ kHz, whereas the sixth-rank ZFSPs could not be resolved in the spectra. A considerable temperature dependence was observed, since at 5 K they obtained $|B_2^0| = 0.860(2)$ GHz.[5] The tetragonal ZFSP B_4^4 was found to show no effect on the spectral shape within the limits of the observed linewidths.[5]

Erdem *et al.*[7] studied by EMR the defect structure of Fe^{3+}-, Cu^{2+}-, Mn^{2+}- and Gd^{3+}-doped bulk $PbTiO_3$ and nano ($\sim$100 nm) powders. They found that the spectra of Gd^{3+}:$PbTiO_3$ nanopowders may be characterized by a '*reduced fine-structure interaction*' (B_2^0 = 0.776 GHz) owing to the reduced crystalline (c/a)-ratio as well as an increased line broadening owing to fine-structure strain ($0.5 \times B_2^0$). For Cu^{2+}:$PbTiO_3$, owing to the reduced c/a-ratio, the SH parameters were found[7] to be considerably varied for the nano-regime. A note of caution is pertinent concerning the terminology used therein.[7] The fine-structure (FS) Hamiltonian, *i.e.*, equivalently ZFS Hamiltonian,[8–10] does not represent an '*interaction*'.[10] The wording '*reduced FS*' may be confusing in this context – it most probably means that only a limited number of admissible ZFSPs (FS parameters), *i.e.*, a truncated ZFS Hamiltonian,[8–10] were employed.

Van Tol *et al.*[6] have also used a truncated tetragonal ZFS Hamiltonian[8–10] omitting the six-rank ZFSPs for numerical simulations of the experimental EMR spectra. The authors[6] stated that Gd^{3+} ions can likely substitute for Pb^{2+} ions because of their similar ionic radius, *i.e.*, 110 pm *vs.* 149 pm. Note that while the values of relative radii[5,6] obey the same trend, their magnitudes differ: Gd^{3+} (97 pm) and Pb^{2+} (120 pm).[5] Some distortions of the host lattice may be expected because of local charge mismatch. However, if displacement of Gd^{3+} ions occurs only along the c-axis, the local axial symmetry would be retained. This simplifying assumption was confirmed by the low-temperature EMR spectrum recorded at 319.2 GHz.[6] The HF-EMR spectra[6] have been simulated yielding a set of SH parameters of axial symmetry: D = +2.544(5) GHz, E = 0, B_4^0 = −0.36 MHz, $g_\parallel$ = 1.9888(2), and $g_\perp$ = 1.9911(2). The conversion relations between the ZFSPs[5,6] were given[6] as $D = 3B_2^0$ and $B_4^0 = 60B_4^0$. Note that some confusion concerning general conversions of ZFSPs exists in the literature – see reviews[9,10,21] reveal some confusion concerning general conversions of ZFSPs in the literature. Table 1 lists the g-factors and ZFSPs determined experimentally at specific temperatures. Unified notation as in eqn (2) and units of 10^{-4} cm^{-1} are adopted in Table 1.

Table 1 Original experimental g_i (dimensionless) and ZFSPs B_k^q (in MHz) and ZFSPs b_k^q converted by us to (10^{-4} cm^{-1}) for the Gd^{3+} centers in $PbTiO_3$

T (K)$^{Ref.}$	G	B_2^0	B_4^0	b_2^0	b_4^0
5 K[5]	1.992 ± 0.002	860	−0.00767	861.0	−0.154
6 K[6]	$g_\parallel$ = 1.9888 $g_\perp$ = 1.9911	848	−0.360	848.6	−7.21
293 K[5]	1.992 ± 0.002	776	−0.00767	776.6	−0.154

Based on structural data,[44–46] indicating the ascend in the local site symmetry around the Gd^{3+} center from tetragonal to cubic symmetry at higher temperatures, the second-rank axial ZFSP B_2^0 should vanish at around 760 K. Table 1 indicates that there is a large difference (almost 50 times) between the reported fourth-rank ZFSPs.[5,6] Presumably, there might be a conversion problem since the difference is close to the factor 60 in the conversion relation $B_4^0 = 60B_4^0$.

3. Crystallographic data and structural phase transitions

Some structural phase transitions have been observed in pure $PbTiO_3$ (PTO) with decreasing or increasing temperature.[47,48] For example, accurate measurements of lattice constants of PTO by Kobayashi *et al.*[47] in the low temperature region have revealed a symmetry descent from tetragonal to orthorhombic or monoclinic phase at 183 K. Two phases in the high temperature region have been detected: a ferroelectric phase (phase II) and a paraelectric phase (phase I) below and above the Curie temperature T_{tr} = 763 K, respectively. Knowledge of the mechanisms of ferroelectric–paraelectric phase transitions is important for in-depth understanding of the physical and electro-mechanical properties of ferroelectric materials. It is worth noting that the reduction in $T_{tr} \approx 700$ K[49] observed in nanopowders was related to a size-driven phase transition associated with a critical mean particle size (16 nm). Raman spectroscopy measurements[48] revealed the structural changes that were ascribed to the cations of $PbTiO_3$ in phase II moving

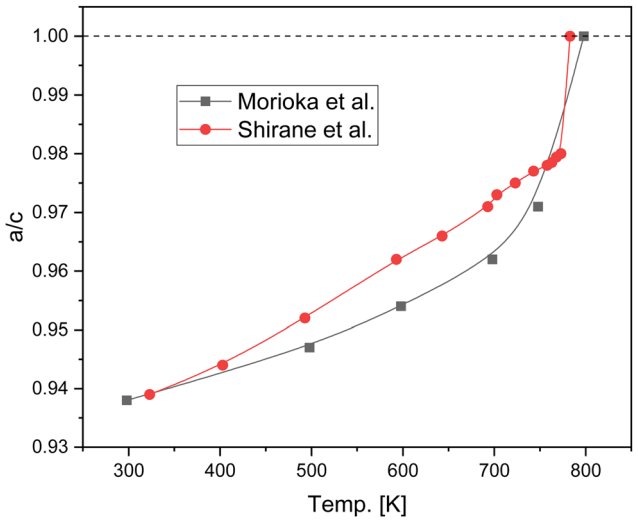

Fig. 1 Variation of the unit-cell parameter ratio a/c with temperature for $PbTiO_3$ plotted using the data.[45,46]

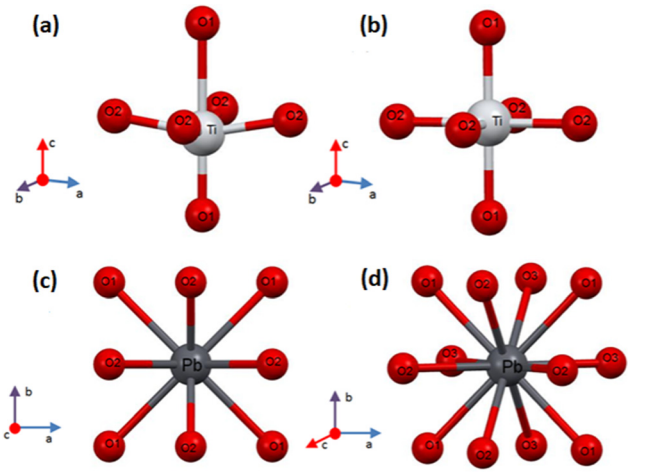

Fig. 2 The $[Ti–O_6]^{8-}$ cluster in $PbTiO_3$: (a) at low temperature in the tetragonal phase; (b) above 763 K in the cubic phase. The $[Pb–O_{12}]^{22-}$ cluster with the Pb^{2+} site surrounded by 12 cubo-octahedrally coordinated O-ligands in $PbTiO_3$; (c) view along the crystallographic c-axis showing only 8 ligands; (d) view after rotation about the b-axis indicating all ligands.

away from the center of the anion lattice, thus creating an inner electric field with spontaneous polarization and a permanent electric moment.

The crystal structure of $PbTiO_3$ in phase II (ferroelectric) below the transition temperature, T_{tr} = 763 K, is tetragonal with the space group C_{4v}^1-$P4mm$, while above T_{tr} in phase I (paraelectric) it is cubic with space group O_h^1-$Pm3m$. The lattice constants (a, c) reported[44] at various temperatures are (in Å) (3.905, 4.156) at room temperature, (3.899, 4.167) at 158 K, (3.895, 4.171) at 90 K, and (3.97, 3.97) at 823 K. Variation of the unit-cell parameter ratio c/a with temperature reported[45,46] is shown in Fig. 1. The X-ray data[46] reveal that increasing content of Gd and Ce dopants increases the lattice tetragonality in $Pb_{0.90}La_{0.15}TiO_3$ films. Unlike this, Barranco *et al.*[51] from their structural and differential scanning calorimetry (DSC) measurements revealed that doping PTO with La^{3+} reduced the tetragonality and cell volume and observed the onset of partial substitution of the rare earth at the B-site (Ti^{4+} site). A similar finding was also obtained in the preceding study,[52] even though the dielectric response indicated no evidence for partial Ti-site occupation of these rare-earth ions. To correlate structural data with spectroscopic EMR data, we employ the two-fold modeling approach outlined above. Hence, first we perform *ab initio* computations to obtain the geometry optimized unit-cell parameters a and c for both pure PTO and Gd^{3+} doped PTO. The variation of the unit-cell parameters (a and c) and the ratio c/a are determined for $Pb_{0.875}Gd_{0.125}TiO_3$ and $PbTi_{0.875}Gd_{0.125}O_3$ in a 2 × 2 × 2 supercell. The rationale for selecting these two compositions is that this choice enables comparative study of the properties of Gd-doped $PbTiO_3$ samples with the dopant ions occupying both the A and B sublattices of the perovskite ABO_3 structure. In this case, not only the effects of Gd but also the effects of substitutions at A and B sublattices may be revealed. Detailed analyses of atomic multiplicity, equivalence, and nonequivalence of the unit cell and supercells are given in Section II of the ESI.†

To discern which cation site A (Pb) or B (Ti) in $PbTiO_3$ is occupied by the dopant Gd^{3+} ions, both sites are considered in our SPM analysis. The structural data, ligand bond lengths and the angular positions of O^{2-} ligands, are determined from our optimized structures for the cation sites Ti^{4+} and Pb^{2+}, respectively, both having tetragonal local site symmetry. These data are listed in Table S1 (all additional materials are given in Section tables and figures of the ESI†) for the $[Ti–O_6]^{8-}$ cluster and Table S2 (ESI†) for the $[Pb–O_{12}]^{22-}$ cluster. Note that the data are expressed in the axis system ($z||c$, $y||b$, $x||a$) and correspond to the tetragonal phase. The structural data for various phases listed in Tables S1 and S2 in the ESI,† which were obtained from the cif files,[44] are depicted in Fig. 2a and b for the $[Ti–O_6]^{8-}$ cluster in tetragonal phase at low temperatures and cubic phase above 763 K. The shift of the Ti^{4+} ion (by about 0.3 Å) from the center of the cluster along the C_4 axis is clearly noticeable in the tetragonal phase. As shown in Fig. 2c and d, the Pb^{2+} site is surrounded by 12 cubo-octahedrally coordinated O-ligands of three kinds: O1, O2, and O3. The relaxed structures after *ab initio* optimization are presented in Fig. S1 and S2 in the ESI† for Ti^{4+} and Pb^{2+} sites, respectively.

4. *Ab initio* computations

4.1. Computational methods

An outline of the major *ab initio* methods utilized is given below, whereas computational details specific for each method invoked in Sections 4.2 to 4.5 are provided in Section III in the ESI.† Two general aspects are worth mentioning. (1) For $Pb_{0.875}Gd_{0.125}TiO_3$ and $PbTi_{0.875}Gd_{0.125}O_3$ structures, as well as simulating vacancy superstructures, several appropriate 2 × 2 × 2 supercells are constructed. The details of the structures are provided in Section II of the ESI.† All the DFT calculations for these constructed structures are performed at

zero temperature. The procedures that allow one to include higher temperatures in DFT computations are discussed in Section III.1 of the ESI,† as recently one of them is used to study the thermoelectric properties of cerium-based compounds.[53,54] (2) The DFT computations are performed for bulk systems only. Nanoparticle computations are much heavier than the bulk computations. The former computations need larger supercells including enough vacuum around the particles. This in turn leads to lower symmetry. Larger supercells and vacuum, as well as lower symmetry would require more expensive computations, which are beyond the scope of this paper.

The structural properties and electronic structures of the compounds under consideration are computed using DFT.[11,12] To this end, the full potential augmented planewaves plus local orbitals (FP-APW + lo) method[55,56] is employed, including spin-polarization and the relativistic spin–orbit coupling (SOC), as implemented in the WIEN2k code.[13,14] For the exchange–correlation term of the Kohn–Sham Hamiltonian, we choose the semilocal Perdew–Burke–Ernzerhof generalized gradient approximation (PBE-GGA) for the optimization and structural properties, whereas for the formation energies and electronic properties, we choose the hybrid functional[57] and set its dimensionless α parameter to 0.25. The reasons for choosing the PBE-GGA and hybrid functional, based on the evidence reported in ref. 58–60, are discussed in Section SIII.2 of the ESI.† Therein, it is also argued, based on ref. 13, 61 and 62, that 0.25 can provide an appropriate choice for the α parameter of the hybrid functional in this work. The details of the relativistic SOC and its effects, based on ref. 63–65, are discussed in Section SIII.3 (ESI†).

In the first Brillouin zone (1BZ), 200 k-points corresponding to a $5 \times 5 \times 5$ Monkhorst-Pack scheme[66] are selected after performing k-point optimizations. The optimizations are performed to theoretically predict the optimized lattice parameters while relaxations are obtained by the minimization of the forces exerted on the atoms having internal parameters in their coordinate positions. Here, the full relaxations are performed by moving (relaxing) the atoms until the forces acting on them, including Hellmann–Feynman forces, become less than our desired criterion, *i.e.*, 1 mRy bohr^{-1}, for all the doped compounds. Computational parameters $R_{MT}K_{max}$ and G_{max} are optimized to be 7 and 12 bohr^{-1}, respectively, where R_{MT} is the smallest muffin-tin radius in the unit cell and K_{max} (G_{max}) determines the cutoff of the Fourier expansion(s) of the wavefunction (charge density and potential). The R_{MT} radii of Pb and Gd are set to 2.5 bohr, and the R_{MT} radius of Ti (O) is adjusted to 1.76 (1.59) bohr. In $Pb_{0.875}Gd_{0.125}TiO_3$ and $Pb_{0.875}Gd_{0.125}TiO_{3-\delta}$ ($PbTi_{0.875}Gd_{0.125}O_3$ and $PbTi_{0.875}Gd_{0.125}O_{3-\delta}$) the R_{MT} radius of Gd is 2.5 (2.17), where δ measures the amount of oxygen vacancies. In order to increase the accuracy of the formation energy calculation we have constructed a supercell for the pure compound similar to supercells constructed for the doped compounds, as well. This ensures that computations for the pure and doped structures are performed on the same footing, which in turn leads to the cancelation of errors and hence to higher accuracy of the computed formation energy.

Here, we also compute and analyze the Bader charges using the quantum theory of atoms in molecules (QTAIM) developed by Bader.[15,16] In the QTAIM,[67] an atom in a molecule or solid is defined as an open system bounded by a surface of local zero flux in the gradient vector field of the electron charge density (ECD), $\rho(r)$. In this work, we employ the QTAIM's definition to interpret chemical bonds between the constituent atoms in Gd:$PbTiO_3$. To this end, we first calculate the Bader electron charges (BECs) of all the atoms inside the pure and doped compounds by using a combination of two codes: the DFT-based WIEN2k,[13,14] and QTAIM-based CRITIC2.[17,18] Using the BECs, we quantitatively determine the valences of the individual atoms and analyze if they are fractional numbers inside their crystalline environments, thus indicating that they differ from their corresponding integer values in the free space. Second, we analyze the BECs to identify the chemical bonds between the constituent atoms. Although we determine the BECs quantitatively, using this procedure we can interpret the chemical bonds only qualitatively. In addition to the BECs, it is possible to extend this study by considering the topology of ECD (TECD) to provide quantitative characterization of the nature of chemical bonds.[68] However, more elaborate calculations based on the TECDs are beyond the scope of this paper.

4.2. DFT optimization

The lattice parameters of the pure and doped compounds in the absence of the oxygen vacancy were optimized by fitting to the Birch–Murnaghan[69] equation of solid state within PBE-GGA. The corresponding energies as functions of volumes are shown in Fig. 3.

In this work, the effects of oxygen vacancies on the structural properties of $PbTiO_3$ are also studied for the following reasons. ABO_3 perovskite oxides, such as $PbTiO_3$, $BaFeO_3$, $BiFeO_3$, and $LiOsO_3$, are an important family of multiferroics compounds.[70–72] Ferroelectric and/or multiferroics properties of $PbTiO_3$ have been extensively studied.[73–77] Fatigue or the loss of switchable polarization under bipolar cycling and dielectric breakdown are two critical issues that have hindered the commercialization of ferroelectric memory devices. The role of oxygen vacancies in fatigue and dielectric breakdown has been a topic of intense research in ferroelectric ABO_3 perovskites like $PbTiO_3$ and $BaTiO_3$. Xiao *et al.*[78] have shown that oxygen vacancies act as donors or n-type dopants for the ferroelectric. Shimada *et al.*[79] have demonstrated that oxygen vacancies induce ferromagnetism in $PbTiO_3$. The effect of oxygen vacancies on the ferroelectricity of the 90° domain wall in $PbTiO_3$ was investigated by Wang *et al.*[80] Feng *et al.*[81] have shown that oxygen vacancies in oxide ferroelectrics can be strongly coupled to the polar order *via* local strain and electric fields, thus holding the capability of producing and stabilizing exotic polarization patterns.

The optimized lattice parameters a and c as well as their ratios c/a together with the bulk moduli B and their pressure derivatives B' are listed in Table 2 for the pristine $PbTiO_3$ compound and the doped $Pb_{0.875}Gd_{0.125}TiO_3$ as well as $PbTi_{0.875}Gd_{0.125}O_3$ compounds. We have computed the lattice

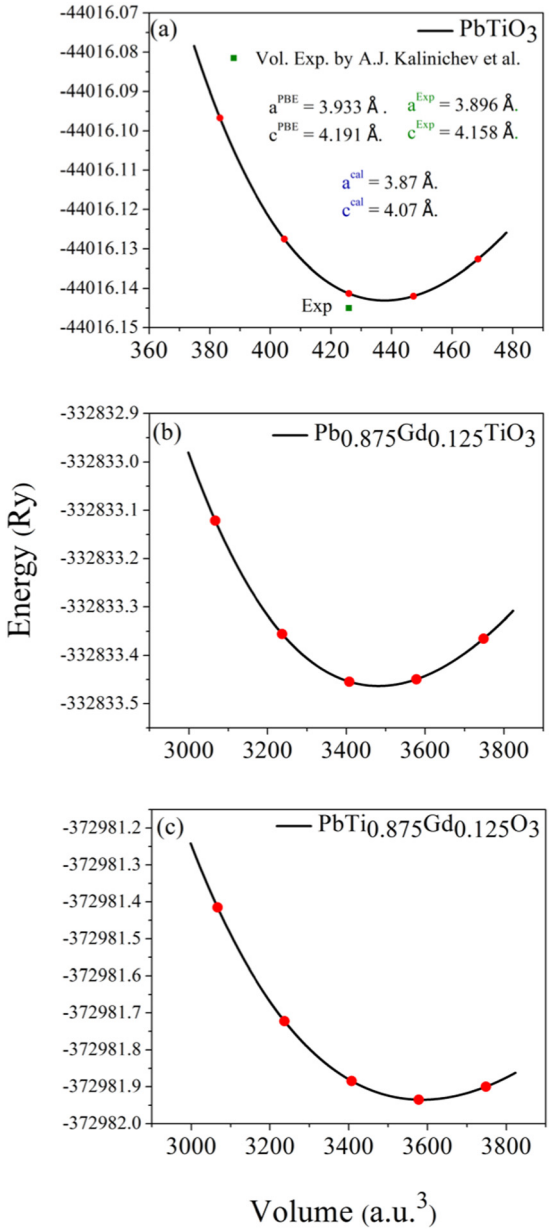

Fig. 3 Energy *versus* volume fitted by the Birch–Murnaghan equation of state within PBE-GGA for (a) pure $PbTiO_3$, (b) $Pb_{0.875}Gd_{0.125}TiO_3$ after doping Gd^{3+} into the pure compound at the Pb-site, and (c) $PbTi_{0.875}Gd_{0.125}O_3$ after introducing Gd^{3+} into the pure compound at the Ti-site. The doped cases are optimized in the absence of the oxygen vacancy. Experimental (exp.) values[83] of lattice parameters for the pristine case are given in (a) for comparison.

parameters of the pure case by the PBE-GGA functional. For comparison the lattice parameters computed by the others[82] within pseudopotential using LDA and the available experimental data[83] are given in Table 2, as well. The comparison shows that our lattice parameters predicted by the PBE-GGA functional are in agreement with the previous theoretical results[82] and experimental data.[83] The results in Table 2 show that the PBE-GGA functional overestimates both lattice constants a and c as compared with experimental data,[83] whereas the LDA functional used in ref. 82 underestimates them. Such trend between the lattice parameters calculated by LDA and PBE-GGA functionals has also been observed for ZrCoBi and ZrRhBi compounds (see Table 1 of ref. 84) and PbS, PbTe, ZnS, and ZnTe (see Table 1 of ref. 85) as well as for $LiRF_4$ (R = Tb, Dy, Ho, Er, Tm, and Yb) compounds (see Table VI in ref. 86). The physical reason for such trend can be related to the fact that the PBE-GGA functional underestimates the Hartree–Fock electron–electron (e–e) correlation, leading to larger lattice parameters, whereas the LDA functional overestimates the e–e correlation, resulting in smaller lattice parameters. Consequently, the localization degree predicted by LDA is smaller than that predicted by PBE-GGA (see ref. 87). Therefore, PBE-GGA predicts that atoms are bonded weaker to each other than in the case of LDA. This weaker bonding estimated by PBE-GGA compared to LDA, in turn, also evidently corroborates the finding that the lattice parameters calculated by PBE-GGA are larger than those calculated by LDA.

The lattice parameters (see Table 2) show that both lattice constants a and c of $Pb_{0.875}Gd_{0.125}TiO_3$ are smaller than the corresponding values of $PbTi_{0.875}Gd_{0.125}O_3$. This implies that the supercell volume expands more when the dopant Gd ions occupy the Ti sites compared to when they occupy Pb sites. This may indicate that bonding of Gd–O states is stronger (weaker) than the bonding of Pb(Ti)–O states. This result is in agreement with Gd atom valences obtained by DFT/*ab initio* computations for the dopant Gd ions substituted in the Pb(Ti) site. Moreover, according to Table S2 (ESI†) we can observe that $Pb–O_{12}$ bond lengths are longer in comparison with Gd–O1 bond lengths while the other bond lengths are almost equal. In contrast, Ti–O1 bond lengths on average are shorter than Gd–O1 by considering Table S1 (ESI†).

The results show that the bulk modulus of the pristine case is smaller (larger) than that of $Pb_{0.875}Gd_{0.125}TiO_3$ ($Pb_{0.875}Gd_{0.125}TiO_{3-\delta}$) in the absence (presence) of the oxygen vacancy. Thus, the pristine case is mechanically harder (softer) than $Pb_{0.875}Gd_{0.125}TiO_3$ ($Pb_{0.875}Gd_{0.125}TiO_{3-\delta}$) in the absence (presence) of the oxygen vacancy. It is worth noting that although the equilibrium lattice parameters can be accurately extracted by fitting the total energy–volume data with an appropriate equation of state, the values computed for the bulk moduli and their pressure derivatives are sensitive to the range of fitting. Therefore, only the qualitative analysis is reliable and we cannot fully trust the quantitative values presented in Table 2. Furthermore, to the best of our knowledge, no experimental results for the bulk moduli and their pressure derivatives of the doped cases have been reported yet; hence our results on Gd^{3+}-doped $PbTiO_3$ may serve as predictions for future studies.

As shown in Table 2, the change of the lattice parameters is quite profound when the same amount of Gd ions substitute for the Pb site or Ti site. It has been observed that the structural changes are directly related with the dopant amount and the type of the dopant as well as the site occupied by the dopant ion. Moreover, the unit-cell volume considerably changes upon Gd^{3+} doping, which arises from the doubling of the lattice

Table 2 The computed lattice parameters a and c (in Å), c/a ratio, and bulk modulus (B) and its pressure derivatives (B') for the pristine $PbTiO_3$ using PBE-GGA and LDA functionals and the doped $Pb_{0.875}Gd_{0.125}TiO_3$, $PbTi_{0.875}Gd_{0.125}O_3$, and $Pb_{0.875}Gd_{0.125}TiO_{3-\delta}$ as well as $PbTi_{0.875}Gd_{0.125}O_{3-\delta}$ using the PBE-GGA functional. The lattice parameters of the latter compound are optimized in the presence of the oxygen vacancy, where the stoichiometric parameter δ is set to $\frac{1}{8} = 0.125$. The results for the pure compound computed by the full-potential (FP) method are compared with the results of the others[82] computed by the pseudopotential (PS) method and the available experimental data.[83] The O-vacancy is around Gd sites for $Pb_{0.875}Gd_{0.125}TiO_{3-\delta}$ ($PbTi_{0.875}Gd_{0.125}O_{3-\delta}$)

Compound	Method	XC	a	c	c/a	B (GPa)	B'	Ref.
$PbTiO_3$	FP	GGA	3.933	4.191	1.066	160.351	4.49	This study
$PbTiO_3$	PS	LDA	3.87	4.07	1.052			82
$PbTiO_3$	Exp.		3.896	4.158	1.067			83
$PbTiO_3$	Exp.		3.905	4.156	1.064			44
$Pb_{0.875}Gd_{0.125}TiO_3$	FP	GGA	7.843	8.387	1.069	162.033	4.59	This study
$Pb_{0.875}Gd_{0.125}TiO_{3-\delta}$ with O-vacancy[a]	FP	GGA	7.879	8.392	1.065	152.284	4.58	This study
$PbTi_{0.875}Gd_{0.125}O_3$	FP	GGA	7.956	8.393	1.055	152.821	4.75	This study
$PbTi_{0.875}Gd_{0.125}O_{3-\delta}$ with O-vacancy[a]	FP	GGA	7.957	8.433	1.056	148.101	4.71	This study

[a] δ = 1/8.

parameters. These changes are more profound for B-site (Ti^{4+} site) occupation. It is important to note that the lattice parameters are doubled since an appropriate 2 × 2 × 2 supercell is used in the *ab initio* computations in order to preserve the stoichiometry.

4.3. Formation energies

Some explanations are pertinent. Enthalpy (H) is related to the internal energy (E), pressure (P), and volume (V) of the system as $H = E + PV$. Our DFT computations are performed at zero pressure. Thus, the total energies are equal to the corresponding free enthalpy energies, *viz.*, $H = E + 0 \times V = E$. Therefore, the enthalpy of the reaction is calculated by considering the total energies. For the gas phase, the pressure is nonzero, but this case is not considered here, since we deal with solid phase only. We have computed the formation energies of the defects, E_f^D, as follows:[88–90]

$$E_f^{D\equiv d} = E(Pb_{0.875}Gd_{0.125}TiO_3) - E(PbTiO_3) + E(Pb) - E(Gd), \quad (3)$$

$$E_f^{D\equiv Gd} = E(PbTi_{0.875}Gd_{0.125}O_3) - E(PbTiO_3) + E(Ti) - E(Gd), \quad (4)$$

$$E_f^{D\equiv V_O} = E(Pb_{0.875}Gd_{0.125}TiO_{3-\delta}) - E(Pb_{0.875}Gd_{0.125}TiO_3) + E(O), \quad (5)$$

$$E_f^{D\equiv V_O} = E(PbTi_{0.875}Gd_{0.125}O_{3-\delta}) - E(PbTi_{0.875}Gd_{0.125}O_3) + E(O), \quad (6)$$

where D stands for either Gd dopant or oxygen vacancy V_O, the first terms in eqn (3)–(6) are the total energies derived from a supercell calculation with dopant or defect doped in the cell and the second terms are the total energies of the ideal supercell. The third and the last terms of eqn (3) and (4)) are the ground state total atomic energies of Pb and Gd (Ti and Gd) atoms, respectively.

For atomic energy computations, we have used a cubic cell with 40 bohr for its lattice constant containing one atom and performed the DFT computations using the APW + lo method. By this way, we have performed the crystal and atomic computations on the same footing to take the advantage of cancelation errors. We have checked and found that 40 bohr selected for the lattice parameter is large enough to avoid interactions of the atom with its neighboring atoms. In the last terms of eqn (5) and (6), E(O) energies are half of $E(O_2)$, *viz.*, $E(O) = \frac{1}{2}E(O_2)$. For the oxygen atom, we take the O_2 molecule as reference, instead of O atoms. Although taking the O_2 molecule as reference has led to bit cumbersome and more expensive computations, we have considered it to increase the accuracy of the computations (see ref. 88).

Furthermore, in addition to the APW + lo code, we have computed the atomic energies using a modified version of the relativistic atomic LSDA code originally written by J. P. Desclaux and Y.-K. Kim.[91] The modified version of the atomic LSDA code is called the LSTART program, as implemented in the WIEN2k code.[13,14] The results computed using the DFT-based APW + lo method are found to be in agreement with the results computed using the LSTART program executed in the initialization part of the WIEN2k code. Therefore, in Table 3 we only provide the atomic energies computed using the APW + lo method together with the total atomic energies of Gd, Pb, Ti, and O atoms obtained computed using the PBE-GGA functional, as well as the total energies of $PbTiO_3$, $Pb_{0.875}Gd_{0.125}TiO_3$, $PbTi_{0.875}Gd_{0.125}O_3$, $Pb_{0.875}Gd_{0.125}TiO_{3-\delta}$, and $PbTi_{0.875}Gd_{0.125}O_{3-\delta}$ compounds computed using the hybrid functional.

The results in Table 3 indicate that the largest (smallest) absolute value of the total energy belongs to the Pb(O) atom among the other elements listed in this table. The computed

Table 3 The atomic total energies (in eV) of Gd, Pb, Ti and O elements computed using PBE-GGA together with the total energies of the 2 × 2 × 2 $PbTiO_3$, $Pb_{0.875}Gd_{0.125}TiO_3$, $PbTi_{0.875}Gd_{0.125}O_3$, $Pb_{0.875}Gd_{0.125}TiO_{3-\delta}$, and $PbTi_{0.875}Gd_{0.125}O_{3-\delta}$ supercells using the hybrid functional

Element	E (eV)	Compound	E (eV)
		$PbTiO_3$	−4790960.935
Gd	−306954.666	$Pb_{0.875}Gd_{0.125}TiO_3$	−4528423.885
Pb	−569493.118	$PbTi_{0.875}Gd_{0.125}O_3$	−5074669.702
Ti	−23227.519	$Pb_{0.875}Gd_{0.125}TiO_{3-\delta}$	−4526369.403
O	−2045.734	$PbTi_{0.875}Gd_{0.125}O_{3-\delta}$	−5072622.267

atomic energies can be sorted as $|E(\mathrm{Pb})| > |E(\mathrm{Gd})| > |E(\mathrm{Ti})| > |E(\mathrm{O})|$, which is consistent with the increment of the atomic numbers of the elements Z, *viz.*, $Z(\mathrm{Pb}) = 82 > Z(\mathrm{Gd}) = 64 > Z(\mathrm{O}) = 8 > Z(\mathrm{Ti}) = 22$. Table 3 reveals that the absolute energy value for the pure $PbTiO_3$ compound decreases due to the introduction of Gd at the Pb-site of the pure compound, *viz.*, $|E(PbTiO_3)| > |E(Pb_{0.875}Gd_{0.125}TiO_3)|$, which is in agreement with $Z(\mathrm{Gd}) = 64 < Z(\mathrm{Pb}) = 82$. This observation applies also in the presence of the oxygen vacancy, *viz.*, $|E(PbTiO_3)| > |E(Pb_{0.875}Gd_{0.125}TiO_{3-\delta})|$. We also notice that after introducing the oxygen vacancy the absolute value of the total energy decreases, *viz.*, $|E(Pb_{0.875}Gd_{0.125}TiO_3) > |E(Pb_{0.875}Gd_{0.125}TiO_{3-\delta})|$. Conversely, we observe that the absolute value of the total energy of the pure $PbTiO_3$ compound increases due to the introduction of Gd into the pure compound at the Ti-site, *viz.*, $|E(PbTiO_3)| < |E(PbTi_{0.875}Gd_{0.125}O_3)|$, which is also in agreement with $Z(\mathrm{Gd}) = 64 > Z(\mathrm{Ti}) = 22$. This observation applies also after removing the oxygen vacancy, $|E(PbTiO_3)| < |E(PbTi_{0.875}Gd_{0.125}O_{3-\delta}|$. In this case, we also note that the total energy decreases due to the introduction of the oxygen vacancy, *viz.*, $|E(PbTi_{0.875}Gd_{0.125}O_{3-\delta}) < |E(PbTi_{0.875}Gd_{0.125}O_3)|$. All these observations validate the overall trends inherent in the results. The formation energies computed using the PBE-GGA functional for doped $PbGdTiO_3$ compounds are presented in Table 4.

Table 4 reveals that the formation energy of the doped Gd^{3+} in the Pb-site is negative, whereas in the Ti-site it is positive. Since our computations are performed at zero pressure, the computed total energies are equal to the corresponding free enthalpy energies. A negative enthalpy of formation energy shows that the formation of a compound is exothermic. This demonstrates that the amount of energy it takes to break bonds is less than the amount of energy that is released when making the bonds. Therefore, the negative value presented in Table 4 shows that $Pb_{0.875}Gd_{0.125}TiO_3$ may be more stable than $PbTi_{0.875}Gd_{0.125}O_3$. This, in turn, indicates that the Pb-site may constitute a more favorable site than the Ti-site for introducing the Gd dopant. However, it is worth noting that the formation energy of the O-vacancy in $Pb_{0.875}Gd_{0.125}TiO_{3-\delta}$ is about 7 eV larger than that of $PbTi_{0.875}Gd_{0.125}O_{3-\delta}$. This, regardless of the signs of the formation energies, indicates that the Ti-site in the presence of the first kind of the O-vacancy, O1, may be a more plausible site than Pb for doping Gd in the presence of the oxygen vacancy. This shows that the O-vacancy can play an important role in changing the location site of Gd from Pb towards Ti in the pristine $PbTiO_3$ compound. However, the *ab initio* results, as aforementioned, show that the formation energy is negative only for the $Pb_{0.875}Gd_{0.125}TiO_3$ composition. For the latter composition, the Gd^{3+} ion is doped at the Pb-site in the absence of the first kind of the O-vacancy, as indicated by O1 in Section 3. The formation energies are calculated to be positive for the other compositions (see Table 4). Therefore, the DFT results, taking the signs of the formation energies as presented in Table 4, show that the most probable position for the substitution of the Gd^{3+} ion is the Pb site. This *ab initio* result is consistent with the experimental observation[5,6,50] and our semiempirical finding, as will be discussed subsequently in Section 5.3.2.

Table 4 The computed formation energies, E_f^D, in eV for the 2 × 2 × 2 supercells of the doped compositions $Pb_{0.875}Gd_{0.125}TiO_3$ and $PbTi_{0.875}Gd_{0.125}O_3$ ($Pb_{0.875}Gd_{0.125}TiO_{3-\delta}$ and $PbTi_{0.875}Gd_{0.125}O_{3-\delta}$) in the absence (presence) of the O-vacancy, V_O. e V_O is around Gd-sites for both $Pb_{0.875}Gd_{0.125}TiO_{3-\delta}$ and $PbTi_{0.875}Gd_{0.125}O_{3-\delta}$ compositions

Defect	Compound	E_f^D (eV)
Gd	$Pb_{0.875}Gd_{0.125}TiO_3$	−1.400
	$PbTi_{0.875}Gd_{0.125}O_3$	18.384
Gd & V_O	$Pb_{0.875}Gd_{0.125}TiO_{3-\delta}$	8.753
	$PbTi_{0.875}Gd_{0.125}O_{3-\delta}$	1.713

4.4. Valences of atoms and stoichiometries of the pure and doped compounds

In our DFT/*ab initio* computations using the WIEN2k code, the charges (valences) of elements in a solid crystal are not set or assumed by default. In the *ab initio* study, instead, the valences of elements in a compound are determined at the end of well-converged SCF calculations.[92–94] The valence of an element in a crystal is not necessarily an integer and can be a fractional number depending on how the quantum states are hybridized to each other. To qualitatively elucidate this aspect, we consider the stoichiometry of the compounds. The stoichiometry of a crystal can be determined by considering the number of atoms that make up the unit cell. The stoichiometry of the pure $PbTiO_3$ crystal is 1 : 1 : 3, because the unit cell of $PbTiO_3$ contains 1 Pb atom, 1 Ti atom, and 3 O atoms.

In analogy to the pure compound, the stoichiometry of the doped compositions can be determined using a three-step procedure outlined in detail in Section SIII.4 in the ESI.† The final results are summarized below. By constructing a supercell and doping Gd at Pb(Ti), the stoichiometry of the $Pb_{0.875}Gd_{0.125}TiO_3$ ($PbTi_{0.875}Gd_{0.125}O_3$) composition in the absence of the oxygen vacancy is determined as 0.875 : 0.125 : 1 : 3 (1 : 0.875 : 0.125 : 3) (see Section SIII.4 in the ESI†). Then, by considering the oxygen vacancy, the stoichiometry of the doped composition in the presence of the oxygen vacancy, $Pb_{0.875}Gd_{0.125}TiO_{3-\delta}$ ($PbTi_{0.875}Gd_{0.125}O_{3-\delta}$), is identified to be 0.875 : 0.125 : 1 : 2.875 : 1.125 (1 : 0.875 : 0.125 : 2.875 : 1.125), where δ = 0.125. Hence, we shall consider the integer or fractional valences of atoms inside the compounds. If we assume that the valences of Pb, Ti, Gd, and O inside the compounds are the same as their corresponding integer values in the free space, *i.e.*, $+2e$, $+4e$, $+3e$, and $-2e$, respectively, then the charges are compensated in the pure $PbTiO_3$, *viz.*, $1 \times (+2e) + 1 \times (+4e) + 3 \times (-2e) = 6e - 6e = 0$. However, this result implies that the net charges are compensated neither in $Pb_{0.875}Gd_{0.125}TiO_3$ ($PbTi_{0.875}Gd_{0.125}O_3$), thus leading to extra $+0.125e$ ($-0.125e$) charges, nor in $Pb_{0.875}Gd_{0.125}TiO_{2.875}\square_{0.125}$ ($PbTi_{0.875}Gd_{0.125}O_{2.875}\square_{0.125}$), thus leading to extra $+0.375e$ ($+0.125e$) charges (see Section SIII.4 in the ESI†). This shows that the so-obtained charges are not balanced for the doped compositions in the presence or absence of the O-vacancy. This implies that the valences of Pb, Ti, Gd, and O atoms inside the doped compositions deviate from their corresponding integer values in the free space, *i.e.*, $+2e$, $+4e$, $+3e$,

and $-2e$. This outcome necessitates quantitative calculations of the valences of the atoms inside the pure and doped compounds presented in Section 4.5.

4.5. Bader electron charges and analyses

We estimate the valences of atoms inside the compounds in question utilizing Bader analysis of the electron density. To this end, we calculate the average Bader electron charges (ABECs) of the atoms inside the pure compound, *i.e.*, $PbTiO_3$, and the doped compositions in the absence of the O-vacancy, *i.e.*, $Pb_{0.875}Gd_{0.125}TiO_3$ and $PbTi_{0.875}Gd_{0.125}O_3$, as well as in the presence of the O-vacancy, *i.e.*, $Pb_{0.875}Gd_{0.125}TiO_{3-\delta}$ and $PbTi_{0.875}Gd_{0.125}O_{3-\delta}$. The computations are performed using DFT[11,12] with PBE-GGA,[95] as implemented in the full-potential-based WIEN2k code,[13,14] plus QTAIM,[15,16] as implemented in the Critic2 code.[17,18]

The computed ABECs are tabulated in Table 5. Wang *et al.*[96] reported the ABECs inside $Pb_{1-x}Cd_xTiO_3$ with x = 0.073 and 0.074 obtained by performing DFT[11,12] with PBE-GGA[97] and by QTAIM[15,16] computations, as implemented in the pseudopotential-based VASP code.[98] The latter ABECs are also presented in Table 5 for comparison.

Analysis of Table 5 reveals what follows. In Table 5, the ABEC of an atom is denoted by q_{Atom}, where the subscript "Atom" refers to Pb, Ti, O, Gd, or Cd. Although the same pure host, *i.e.*, $PbTiO_3$, is studied by us and in ref. 96, we must be careful and expect less than excellent consistency between the results. Some reasons for this expectation arise from the following facts. The impurities, *i.e.*, Gd and Cd, the concentrations, *i.e.*, x = 0.125 and (0.073 or 0.074), and the computational methods, *i.e.*, full potential and pseudopotential, as well as the codes, *i.e.*, WIEN2k and VASP, are different in our study and those in ref. 96, respectively. Moreover, the valence of dopant Cd, like its host Pb, is +2e, whereas the valence of the dopant Gd, *i.e.*, +3e, differs from that of the host Pb. However, the results are acceptably comparable despite these differences (see Table 5), thus indicating to what extent our results can reproduce correct ABECs.

We note that all the q_{Atom} values are fractional numbers for Pb, Ti, O, Gd, or Cd for the pure compound, Gd-doped compositions independent of the O-vacancy, and Cd-doped compositions (see Table 5). These fractional ABECs confirm our predictions based on the stoichiometry of the doped compositions in Section 4.4. To validate our computed ABECs, let us investigate whether the atomic charges can balance each other inside the crystalline environments, taking the compounds' stoichiometry into account. To this end, we evaluate the stoichiometric neutralization (SN) (see Table 5). For example, we find that the SN for the pure $PbTiO_3$ compound almost vanishes, *viz.*, $SN = q_{Pb} + q_{Ti} + 3q_O = 1.3815e + 2.2043e + 3 \times (-1.1947)e = 0.0017e \approx 0$. This insignificant SN verifies to what extent the neutrality of the unit cell of the pure compound is satisfied. This, in turn, also confirms that the charges can be well balanced by considering the stoichiometry of the pure $PbTiO_3$ and the fractional q_{Atom} values of 1.3815e, 2.2043e and $-1.1947e$ for the constituent Pb, Ti, and O atoms, respectively.

In analogy to the pure systems, we evaluate the SN values for the doped compositions (see Table 5). The small SN values (a) verify the neutrality of the supercells of the doped compositions with and without O-vacancy and (b) corroborate that if the fractional Bader charges and stoichiometry are considered, the charges can be well balanced also in the supercells of the doped compositions. For $Pb_{1-x}Cd_xTiO_3$ with x = 0.073 and 0.074, we also evaluate the corresponding SN values using the Bader charges[96] listed in Table 5. We find the latter SN values also to be very small, which confirms that the valence of the atoms inside the crystalline environments can be fractional numbers, as well reproduced by the Bader's method.

Additionally, to estimate the amount of covalent character in the chemical bonds, we evaluate the deviations of q_{Atom}, as computed in the crystalline environments of the pure and doped compounds, from their nominal values in free space $|\Delta q_{Atom}| = |q_{Atom}^{crystal} - q_{Atom}^{freespace}|$, where the nominal values of $q_{Atom}^{freespace}$ are taken to be +2e for Pb, +4e for T, $-2e$ for O, +3e for Gd, and +2e for Cd (see Table 5). It is well-known that the larger the deviation $|\Delta q_{Atom}|$, the larger the deviation between the ionic and covalent bond, and thus the stronger the degree of covalency.[96,99,100] If the deviation $|\Delta q_{Atom}| = 0$, a pure ionic bond between two atoms can occur, because in this case the valence electron(s) are entirely transferred between atoms, leading to a positively charged cation and a negatively charged anion. The larger nonzero deviations $|\Delta q_{Atom}|$ are equivalent to transferring and as a result sharing more electrons in the bonds, which indicates an increase of the covalent bonds as compared to the pure ionic bonds.

Table 5 Bader electron charge of atom q_{Atom} in (e) inside the pure compound $PbTiO_3$ and the doped compositions in the absence (presence) of the O-vacancy, $Pb_{0.875}Gd_{0.125}TiO_3$ and $PbTi_{0.875}Gd_{0.125}O_3$ ($Pb_{0.875}Gd_{0.125}TiO_{3-\delta}$ and $PbTi_{0.875}Gd_{0.125}O_{3-\delta}$). The columns are denoted as defined in Section 4.5. The asterisk * denotes the results computed by us

Compound	q_{Pb} (e)	$\|\Delta q_{Pb}\|$ (e)	q_{Ti} (e)	$\|\Delta q_{Ti}\|$ (e)	q_O (e)	$\|\Delta q_O\|$ (e)	q_{dop} (e)	$\|\Delta q_{dop}\|$ (e)	SN (e)	Ref.
$PbTiO_3$	+1.3815	0.6185	+2.2043	1.7957	−1.1947	0.8053			0.0017	*
$Pb_{0.875}Gd_{0.125}TiO_3$	+1.3754	0.6246	+2.1759	1.8241	−1.2316	0.7684	+2.2798	0.7202	−0.0304	*
$PbTi_{0.875}Gd_{0.125}O_3$	+1.3633	0.6367	+2.3592	1.6408	−1.2286	0.7714	+2.0706	0.9294	0.0006	*
$Pb_{0.875}Gd_{0.125}TiO_{3-\delta}$	+1.2282	0.7718	+2.2658	1.7342	−1.2589	0.7411	+2.0698	0.9302	−0.0201	*
$PbTi_{0.875}Gd_{0.125}O_{3-\delta}$	+1.3306	0.6694	+2.1706	1.8294	−1.1994	0.8006	+1.9751	1.0249	0.028	*
$Pb_{0.927}Cd_{0.073}TiO_3$	+1.3740	0.6260[a]	+2.1806	1.8194[a]	−1.1841	0.8159[a]	+1.3114	0.6886[a]	−0.0023[a]	96
$Pb_{0.926}Cd_{0.074}TiO_3$	+1.3722	0.6278[a]	+2.1789	1.8211[a]	−1.1819	0.8181[a]	+1.2974	0.7026[a]	−0.0001[a]	96

[a] This datum is extracted from the Bader electron charges reported in ref. 96.

Therefore, analysis of the Bader charge may then describe the degree of charge transfer between the cations and the anions.[100] Using the same strategy, Michele Pavone *et al.*[99] have argued that since the effective charges of La in $LaMO_3$ (M = Cr, Mn, Fe, Co) are much closer to the ionic limit of +3*e*, lanthanum is more ionic than the transition metal cations. Similarly, here, we notice that $|\Delta q_{Pb}|$ is less than that of the other atoms in the pure and doped compounds. This result is in agreement with the results reported for $Pb_{1-x}Cd_xTiO_3$ with $x = 0.073$ and 0.074 in ref. 96 In turn, a smaller value of $|\Delta q_{Pb}|$ implies that the effective Bader charge of Pb is equivalently closer to its ionic limit of +2*e* than that of all the other atoms in the pure and doped composition. Therefore, Pb is more ionic than Ti, O, and Gd atoms in the pure and doped cases.

These results also show that $|\Delta q_{Pb}|$ in the pure $PbTiO_3$ is the smallest deviation as compared to $|\Delta q_{Pb}|$ in the doped cases. This means that the ionic character of Pb can be reduced by doping Gd. The values of $|\Delta q_{Pb}|$ show that in the absence of the O-vacancy the Pb bond is more ionic if Gd is doped at Pb than at the Ti site, *viz.*, $|\Delta q_{Pb}| = 0.6246e$ in $Pb_{0.875}Gd_{0.125}TiO_3$ is less than $|\Delta q_{Pb}| = 0.6367e$ in $PbTi_{0.875}Gd_{0.125}O_3$. However, the direction of the inequality is reversed in the presence of the O-vacancy, *i.e.*, the Pb bond with O-vacancy is less ionic when Gd is doped at Ti than at the Pb site, $|\Delta q_{Pb}|_{Pb_{0.875}Gd_{0.125}TiO_{3-\delta}} = 0.7718e > |\Delta q_{Pb}|_{PbTi_{0.875}Gd_{0.125}O_{3-\delta}} = 0.6694e$. The results show that if the Gd is doped at the Ti site in the presence of the O-vacancy, $|\Delta q_{Ti}|$ reaches values up to 1.8294*e*, which is the largest $|\Delta q_{Ti}|$ presented in Table 5. Hence, the Ti atom in $PbTi_{0.875}Gd_{0.125}O_{3-\delta}$ can constitute the strongest covalent bond as compared to the other atoms in the pure compound and the other doped compositions. Moreover, we observe that $|\Delta q_{Ti}| > |\Delta q_{Atom}|$ for "Atom" = Pb, O in the pure compound and for "Atom" = Pb, O, Gd for the doped compositions. This finding is consistent with the results reported for $Pb_{1-x}Cd_xTiO_3$ with $x = 0.073$ and 0.074 in ref. 96. This confirms that the degrees of covalency for Ti bonds are higher than those for the other atoms in the systems presented in Table 5. Furthermore, $|\Delta q_O| > |\Delta q_{Pb}|$ in most of the cases except for $Pb_{0.875}Gd_{0.125}TiO_{3-\delta}$.

Therefore, in addition to the ionic Pb bonds discussed above, Ti and O can be bonded covalently. Further, the degrees of Ti–O covalent bonds across the compounds can be sorted from the highest to the lowest as follows: $|\Delta q_{Ti}| + |\Delta q_O| = 1.8294e + 0.8006e = 2.6300e > 1.7957e + 0.8053e = 2.6010e > 1.8241e + 0.7684e = 2.5925e > 1.7342e + 0.7411e = 2.4753e > 1.6408e + 0.7714e = 2.4122e$, corresponding to the series of compounds $PbTi_{0.875}Gd_{0.125}O_{3-\delta}$ → $PbTiO_3$ → $Pb_{0.875}Gd_{0.125}TiO_3$ → $Pb_{0.875}Gd_{0.125}TiO_{3-\delta}$ → $PbTi_{0.875}Gd_{0.125}O_3$, respectively. Therefore, in agreement with the results reported on $PbTiO_3$ by Pöykkö and Chadi,[101] we notice that the bondings in the pure compound and the doped compositions are a mix of ionic and covalent bonds where most of the covalent contributions originate from Ti–O bonds. The values of $|\Delta q_{Gd}|$ show that the bonds of the dopant depend on both the substitution site and the presence of the O-vacancy around it. These results show that the degree of the ionic (covalent) Gd bond decreases (increases) as $|\Delta q_{Gd}| = 0.7202e > 0.9294e > 0.9302e > 1.0249e$, corresponding to the series of compounds $Pb_{0.875}Gd_{0.125}TiO_3PbTi_{0.875}Gd_{0.125}O_3Pb_{0.875}Gd_{0.125}TiO_{3-\delta}PbTi_{0.875}Gd_{0.125}O_{3-\delta}$, respectively. By substituting Gd at the Pb-site, the changes of $|\Delta q_{Pb}|$ and $|\Delta q_{Ti}|$ as compared to the pure case are small and less than that of $|\Delta q_O|$. However, by substituting Gd at the Ti-site only, the change of $|\Delta q_{Pb}|$ as compared to the pure case is small and less than those of $|\Delta q_{Ti}|$ and $|\Delta q_O|$.

It is generally accepted that ionic bonds can be stronger than covalent bonds, because in ionic (covalent) bonds a complete transfer (only sharing) of electrons can occur between atoms to constitute a stable compound. In the absence of the O-vacancy, the value of $|\Delta q_{Pb}|$ for $Pb_{0.875}Gd_{0.125}TiO_3$ is smaller than that for $PbTi_{0.875}Gd_{0.125}O_3$, leading to a more ionic character, thus possibly stronger Pb bonds for the former than the latter doped composition. This situation is reversed in the presence of the O-vacancy, *i.e.*, the value of $|\Delta q_{Pb}|$ for $PbTi_{0.875}Gd_{0.125}O_{3-\delta}$ is smaller than that for $Pb_{0.875}Gd_{0.125}TiO_{3-\delta}$, leading to a more ionic character, and thus possibly stronger Pb bonds for $PbTi_{0.875}Gd_{0.125}O_{3-\delta}$ than $Pb_{0.875}Gd_{0.125}TiO_{3-\delta}$.

Therefore, one may conclude that in the absence of the O-vacancy the Pb-site may be more plausible than the Ti-site for doping Gd, whereas in the presence of the O-vacancy the Ti-site may be more plausible than the Pb-site for doping Gd. This conclusion drawn based on the bonding strength is consistent with the conclusion drawn based on formation energies in Section 4.3. Despite this consistency, it is worth reemphasizing that the above Bader analyses are solely performed qualitatively. However, quantitative calculations based on the topology of electron charge density are beyond the scope of this paper.

5. Modelling of ZFS parameters for Gd^{3+}:$PbTiO_3$

5.1. Superposition model (SPM) analysis

The semiempirical SPM analysis enables modeling of ZFSPs parameters for a given defect structure and thus correlating the structural and EMR or optical spectroscopy data (for references, see, *e.g.*, reviews[19–21]). SPM has proved very useful in probing the local structure and configuration of the paramagnetic ions located at specific sites in host lattices.[102–104] Since the theoretical framework for SPM/ZFSP analysis has been provided,[19–21] for the sake of brevity, we omit the details here. For completeness, general explicit SPM/ZFSP expressions for the Gd^{3+} ion coordinated by n-ligands are listed in Section I in the ESI† together with explanations of the symbols used.

Here, we employ SPM analysis for modeling ZFS parameters (for short SPM/ZFSP) obtained from EMR spectra as well as for determination of the local structure and the most likely positions of the Gd^{3+} ions in the $PbTiO_3$ host at various temperatures. SPM ZFSPs are predicted by utilizing structural data around a paramagnetic ion, *i.e.* taking only the nearest-neighbor into account, and specific model parameters. The SPM approach has an important advantage, since it can be applied to a sample that might be in various structural forms.

The SPM predicted ZFSPs are matched with the experimental ones to determine the possible structural changes around that paramagnetic center. In our study, we use the experimental ZFSPs obtained for Gd-doped PTO nanostructures,[5–7] which reflect the size/surface effects occurring in these nanostructures.

Here, we utilize the general SPM expressions[105] and the explicit ZFSP expressions[106,107] suitable for Gd^{3+} ions in 6- and 12-coordinated ligand complexes exhibiting tetragonal symmetry (see the ESI†). Several different model parameter values have been adopted in the literature for SPM analysis of the Gd^{3+}–O^{2-} complexes. To make judicious selection of the model parameter sets to be used as input for our SPM/ZFSP calculations, available literature data are compiled in Table 6. It should be noted that sixth-rank ZFSPs were hardly studied, since they have usually quite smaller values than the second- and fourth-rank ZFSPs. Only two sets of the sixth-rank model parameters have been employed in SPM analysis (Table 6). In view of the data in Table 6, it seems reasonable to adopt the following model parameters: $\bar{b}_2(R_0) = -2500 \times 10^{-4}$ cm^{-1}, $t_2 = 4$, $\bar{b}_4(R_0) = 8 \times 10^{-4}$ cm^{-1}, $t_4 = 4$, $\bar{b}_6(R_0) = -0.1 \times 10^{-4}$ cm^{-1}, $t_6 = 12$ with $R_0 = R_{avg} = 0.2466$ nm.

In subsequent sections, we consider several possible structural models for the Gd^{3+} centers based on correlation between experimental EMR data and the SPM-calculated ZFSPs. It is important noting that in the semiempirical modeling approaches like SPM the ligand distances may be independently changed on particular bonds, whereas ligand replacement may also be introduced, *e.g.*, MX_6 to MX_5Y_1. Such structural modifications induce variations of the electronic density of each bond. Thus, when applying SPM, it is necessary to adopt different sets of SPM parameters for different ligands either in a single ligand configuration like MX_6 or in a double ligand configuration like MX_5Y_1. Also, SPM has some limitations when including vacancies in modeling. Although it is possible to consider the role of a nearby ligand vacancy (by treating it as an additional 'ligand'), we can consider only indirectly (via modifications of the model parameters) a remote cation vacancy that may create internal effects in the local structure. For example, it was reported that the internal field due to the vacancy has a key role in explaining the different optical spectrum shown by MgO: Cr^{3+} associated with the Mg-vacancies along ⟨100⟩ or ⟨110⟩ directions.[116] It is well known that the oxygen (O)-vacancies are significant defects in perovskite oxides and are responsible for material properties, *e.g.*, ionic conductivity in electrochemical devices.[49,117] The role of an O-vacancy in the structure is taken into account in subsequent sections.

For comparison of second- and fourth-rank ZFSPs experimentally determined in ref. 5 and 6 as well as the sixth-rank ones, as calculated in this study, the experimentally determined ZFSPs in various other crystals are listed in Table 7. As seen, the temperatures at which the experimental spectra were obtained are provided only in some sources. Theoretical analyses of these systems have also been carried out. The spin-Hamiltonian parameters including sixth-rank ZFSPs have been calculated from a diagonalization of energy matrix method for Gd^{3+}:$MSiO_4$ (M = Hf, Zr, Th) systems,[118] Gd^{3+}:YMO_4 (M = V, P, As) systems,[119] and Gd^{3+}:$SrTiO_3$ system[120] to analyze the defect structure of Gd^{3+} centers at tetragonal host sites.

Some important features may be noted concerning the data in Table 7. First, the sign of b_2^0 is negative for Gd^{3+} centers in all these crystals unlike in $PbTiO_3$ (see Table 1). Second, the value of b_4^0 is quite small and negative, except for $Pr_{1.98}Gd_{0.02}CuO_4$ and $YBa_2Cu_3O_{6+y}$ ($y = 0.06$), being generally around 1% of that of b_2^0, which is consistent with b_4^0 in $PbTiO_3$. It is also common that $b_4^4 > b_4^0$, except for $SrTiO_3$ at 77 K. Third, both b_6^0 and b_6^4 are usually positive and very small, being almost zero. The comparison of our calculated ZFSPs with these experimental data will be discussed in subsequent sections.

5.2. SPM/ZFSPs calculated using the DFT-geometry optimized structural data

We first started our SPM calculations to determine the ZFSPs for Gd^{3+} ions in PTO using the optimized structural data obtained from the *ab initio* computations for four structural models (see Tables S1, S2, and S5 in the ESI†). These models include the Gd^{3+} ion substituted for the (i) Ti-site, (ii) Pb-site, (iii) Ti-site with an O-vacancy, and (iv) Pb-site with an O-vacancy. It is important to note that the results of the DFT computations indicate some structural changes in each of these models. The most profound change occurs in the ligand lengths when the Gd^{3+} ion replaces for the Ti^{4+} ion. In model (i) it appears that the Gd^{3+} ion moves up increasing the shorter O1 ligand length by about 30% as well as that of O2 ligands by 7%. This is reasonable in terms of the larger size of the Gd^{3+} ion

Table 6 Model parameters reported in the literature as adopted in SPM analysis for Gd^{3+} ions in various ligand configurations (ALST stands for $NH_4La(SO_4)_2{\cdot}4H_2O$; NA means data are not available)

$\bar{b}_2(R_0)$	$\bar{b}_4(R_0)$	$\bar{b}_6(R_0)$	Units	t_2	t_4	t_6	R_0 (Å)	System	Ref.
−0.2000 ± 0.050	NA	NA	cm^{-1}	2.5 ± 1.5	NA	NA	2.699	ABF_3-type perovskites	108
−0.1810	0.0009	NA	cm^{-1}	2.5	4	NA	2.466	$CaWO_4$	109
−0.1810	0.0019	NA	cm^{-1}	0.8	16.6	NA	NA	YAG	19 and 110
−0.1810	0.0019	−0.00001	cm^{-1}	0.8	16.6	12	2.3942	$YBa_2Cu_3O_{6+x}$	111
−4.281 ± 0.013	0.020	NA	GHz	8.5 ± 1.0	34	NA	2.755	ALST	112
−0.1428 ± 0.0004	0.0007	NA	cm^{-1}	8.5 ± 1.0	34	NA	2.755	ALST	
−4.457/−5.472	0.021	NA	GHz	8.5	14	NA	NA	RF_3	113
−0.1487/−0.1826	0.0007	NA	cm^{-1}	8.5	14	NA	NA	RF_3	
−0.2800	NA	NA	cm^{-1}	2	NA	NA	2.42	$CaCO_3$/$PbCO_3$	114
−0.2000	−0.00033	0.0002	cm^{-1}	2.5	4	4	2.379	CaO	115

Table 7 The ZFSPs determined experimentally for Gd^{3+} in various crystals (in 10^{-4} cm^{-1}) (NA means data are not available)

Crystal/ZFSPs	b_2^0	b_4^0	b_4^4	b_6^0	b_6^4	Temp. (K)	Ref.
$SrTiO_3$	−362.5(2)	−3.24(50)	−4.2(5)	1.4(5)	−0.69(50)	4.2	111
$SrTiO_3$	−233.6(5)	−4.8(5)	−2.5(3)	−0.25(50)	0.1(5)	77	121
$ZrSiO_4$	−352.6(1)	−7.6(3)	64.2(7)	0.61(3)	1(1)	NA	112
$HfSiO_4$	−307.3(1)	−9.14(3)	63.5(12)	0.63(3)	0(1)	NA	122
$ThSiO_4$	−297.0(1)	−6.78(3)	30.5(6)	0.43(3)	0(1)	NA	122
YVO_4	−441.6(2)	−1.5(2)	41.5(4)	0.8(6)	0.0(2)	NA	123
YPO_4	−727.9(1)	−4.1(2)	21.2(4)	0.4(1)	0.0(2)	NA	123
$YAsO_4$	−316.5(2)	−4.2(1)	46.5(2)	0.4(5)	0.0(2)	NA	123
$Pr_{1.98}Gd_{0.02}CuO_4$	−400	−30	300	0	0	NA	124
$YBa_2Cu_3O_{6+y}(y = 0.06)$	−423.6	−61.9	263.5	0.50	71.1	77	125

Table 8 The tetragonal ZFSPs (in 10^{-4} cm^{-1}) calculated using the optimized structural data obtained from the *ab initio* computations for various structural models

Model/ZFSPs	b_2^0	b_4^0	b_4^4	b_6^0
(i) Ti-site	333.9	42.0	234.8	−0.46
(ii) Pb-site	1248.7	−8.74	−56.3	−0.008
(iii) Ti-site with O-vacancy	1993.3	24.2	197.4	−0.60
(iv) Pb-site with O-vacancy	478.7	−12.0	−9.05	−0.063

and the less resultant attraction force between Gd^{3+} and O^{2-} compared to that between Ti^{4+} and O^{2-}. In model (ii) it appears that the O_{v1} vacancy results in a slight relaxation in the $[Ti–O_6]^{8-}$ cluster by about 3% expansion in the ligand lengths of O2 as compared to model (i). Unlike models (i) and (ii), the substitution of the Gd^{3+} ion for the Pb^{2+} site (model (iii)) induces much smaller distortions in the $[Pb–O_{12}]^{22-}$ cluster. However, in the case of model (iv), the presence of O_{v1} leads to a very significant distortion in the ligand angle of O2 ligands, by pushing them up along the *c*-axis by about 18° (see Table S5 in the ESI†). The SPM results for the four structural models are listed in Table 8.

Analysis of Table 8 enables the following conclusions to be drawn. Concerning the Ti-site substitutions, b_2^0 obtained for model (i) is one-third of the experimental one, while b_4^0 is much higher (see Table 1), whereas b_2^0 obtained for model (iii) increases almost six times, while b_4^0 decreases to almost half of that in model (i). Concerning the Pb-site substitutions, for the model (ii) so-obtained values of b_2^0 and b_4^0 are quite comparable to the experimental ones, whereas for the model (iv) so-obtained value of b_2^0 is about half of the experimental b_2^0 value, whereas the signs of the computed and experimental b_4^0 values agree.

In subsequent sections, we present the results of further SPM calculations to explore the change of the local structure around the Gd^{3+} centers as well as the change of the ZFSPs with temperature.

5.3. Variation of SPM/ZFSPs with temperature

5.3.1. Structural model assuming Gd ions at Ti-sites. In addition to the results in Table 8, further SPM calculations for the Gd^{3+} center at the Ti site in $PbTiO_3$ using the structural parameters of the host given in Table S3 in the ESI† yielded the ZFSPs at RT as (in 10^{-4} cm^{-1}) $b_2^0 = -281.25$, $b_4^0 = 1029.12$, $b_4^4 = 2926.79$, $b_6^0 = -55.04$, and $b_6^4 = 133.39$ at 10 K, whereas $b_2^0 = -1236.6$, $b_4^0 = 61.38$, $b_4^4 = 324.55$, $b_6^0 = -4.92$, and $b_6^4 = 15.21 \times 10^{-4}$. In the cubic phase, the calculated ZFSPs are (in 10^{-4} cm^{-1}) $b_4^0 = 66.69$, $b_4^4 = 333.47$, $b_6^0 = -1.01$, and $b_6^4 = 21.28$. Comparison of these ZFSP values with the experimental ones listed in Table 1 indicates that the Ti^{4+} site is not viable for Gd^{3+}

Table 9 The SPM calculated ZFSPs of the Gd^{3+} center at the Pb^{2+} site in $PbTiO_3$ and local structural parameters of the O-ligands in the $[Pb–O_{122}]^{22-}$ cluster at various temperatures; b_k^q in (10^{-4} cm^{-1}), R_i in (Å), and θ_i in (°)

T (K)	b_2^0	b_4^0	b_4^4	b_6^0	b_6^4	R_1	R_2	R_3	θ_1	θ_2	θ_3
10	861.1	−9.63	−6.94	−0.027	−1.63	2.7581	2.5412	3.3281	83.72	126.76	40.34
30	855.3	−9.63	−7.04	−0.027	−1.63	2.7581	2.5414	3.3277	83.74	126.79	40.35
80	849.0	−9.64	−7.14	−0.026	−1.63	2.7582	2.5417	3.3271	83.76	126.82	40.37
120	836.7	−9.65	−7.34	−0.026	−1.63	2.7583	2.5422	3.3261	83.81	126.88	40.39
160	827.8	−9.65	−7.48	−0.025	−1.63	2.7584	2.5428	3.3249	83.84	126.93	40.41
200	812.6	−9.66	−7.69	−0.024	−1.63	2.7587	2.5433	3.3237	83.89	127.00	40.44
260	807.9	−9.66	−7.76	−0.024	−1.62	2.7589	2.5441	3.3222	83.90	127.02	40.45
293	806.8	−9.66	−7.77	−0.024	−1.62	2.7589	2.5442	3.3219	83.91	127.02	40.45
300	804.9	−9.67	−7.78	−0.024	−1.62	2.7590	2.5441	3.3217	83.91	127.03	40.45
425	735.8	−9.75	−8.72	−0.020	−1.62	2.7594	2.5452	3.3147	84.18	127.39	40.62
520	660.7	−9.79	−9.90	−0.015	−1.61	2.7601	2.5492	3.3062	84.47	127.77	40.80
620	468.5	−9.83	−12.80	−0.002	−1.55	2.7625	2.5618	3.2807	85.19	128.74	41.22
685	363.3	−9.81	−14.26	0.003	−1.52	2.7637	2.5681	3.2679	85.55	129.23	41.33
720	273.4	−9.80	−15.47	0.008	−1.48	2.7649	2.5744	3.2551	85.86	129.64	41.40
752	30.9	−9.64	−18.44	0.020	−1.40	2.7687	2.5927	3.2167	86.66	130.70	41.54
~765	0	−10.13	−20.85	0.045	−1.00	2.807	2.807	2.807	90	135	45

substitution. However, we have carried out some further SPM calculations for this site by direct matching of the distortions of the ligands' lengths and angles with the experimental ZFSPs. We note that matching is only achievable for b_2^0, but not for b_4^0, even though we consider all admissible distortion models. This certainly reveals that the Gd^{3+} ion does not substitute for the Ti^{4+} site in $PbTiO_3$. Actually, both the effective charge mismatch (3+ *vs.* 4+) and a large ionic radii disparity between Gd^{3+} (97 pm) and Ti^{4+} (68 pm) clearly support this finding.

Next, we have considered the possible presence of O-vacancy defects (O_{vi}) around the Ti^{4+} site. Since there are two types of O-ligands in the TiO_6 complex, two O1 along the C_4-axis and four O2 in the *ab*-plane (see Fig. 3 and Table S1 in the ESI†), we have carried out SPM calculations for both possible options: O_{v1} and O_{v2}. Besides, due to the different ligand length between each of the two O1-ligands and the central Ti^{4+} ion, it is required to consider the presence of O_{v1} separately as O_{v1}^{up} (longer O1) and O_{v1}^{down} (shorter O1). Using the structural data of the host structure at RT we computed the ZFSPs as (in 10^{-4} cm^{-1}): $b_2^0 = 2386.11$, $b_4^0 = 37.35$, $b_4^4 = 288.98$, $b_6^0 = -2.39$, and $b_6^4 = 7.26 \times 10^{-4}$ for O_{v1}^{up}, and $b_2^0 = 6087.77$, $b_4^0 = 25.50$, $b_4^4 = 288.98$, $b_6^0 = -0.20$, and $b_6^4 = 7.26 \times 10^{-8}$ for O_{v1}^{down}, whereas $b_2^0 = -281.25$, $b_4^0 = 1029.12$, $b_4^4 = 2926.79$, $b_6^0 = -55.04$, and $b_6^4 = 5.44 \times 10^{-8}$ for the O_{v2} case. Further calculations by taking into account the local distortions of R_i and θ_i have been done for each of the three vacancy cases at this site, as well. Note that any possible

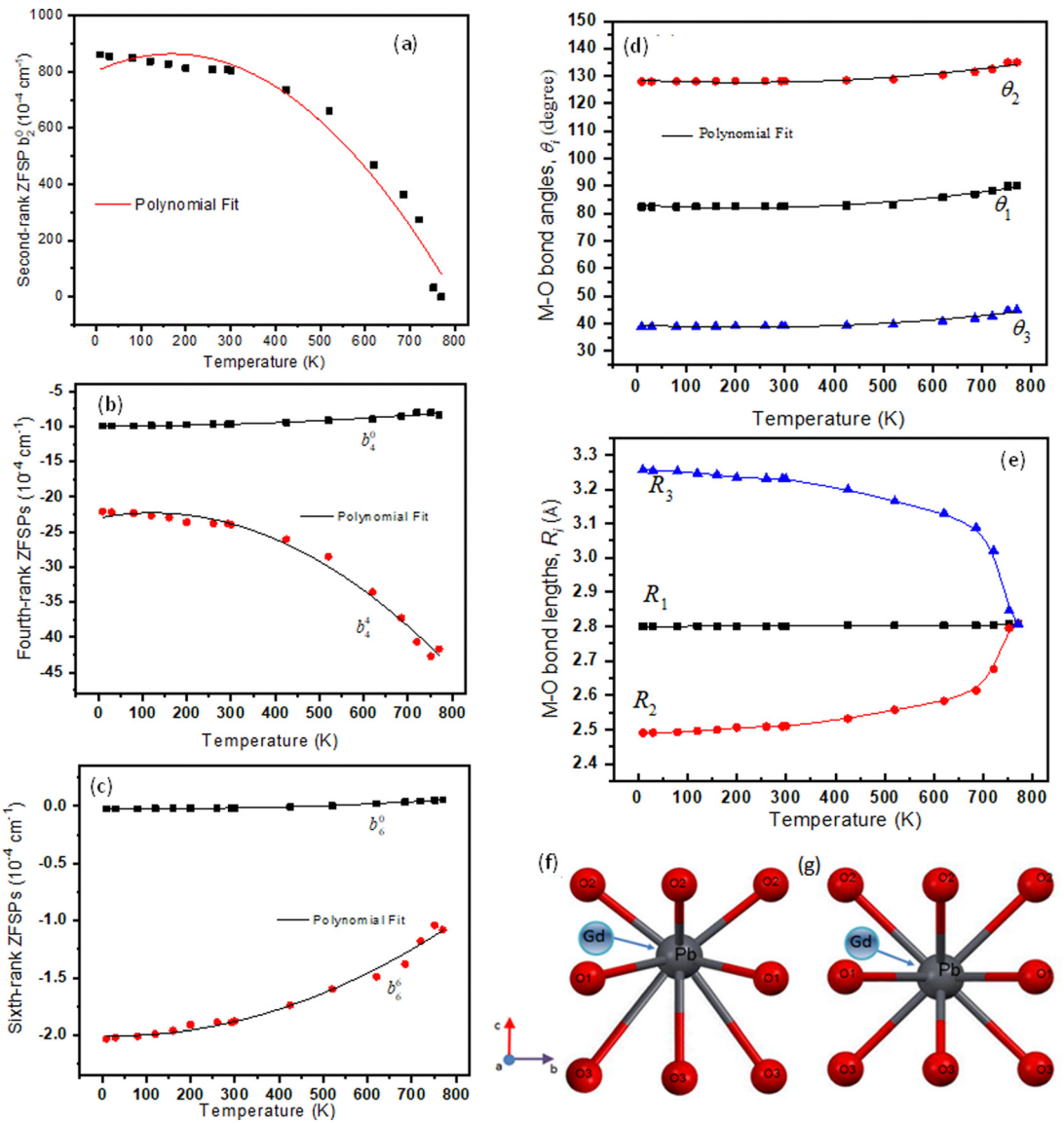

Fig. 4 The variation of ZFSPs: (a) second-rank, (b) fourth-rank, and (c) sixth-rank for Gd^{3+} in $PbTiO_3$ with temperature in the range of 10–765 K. The polynomial curve that fits best the data of each parameter is indicated by a continuous line. Temperature dependence determined using SPM for Gd^{3+} in $PbTiO_3$: (d) the M–O bond angles (θ_i) from the tetragonal C_4-axis and (e) the M–O bond lengths (R_i) of the Pb^{2+} site after Gd^{3+} substitution. Configuration of the cluster $[Gd–O1_2]^{21-}$: (f) at low temperatures (tetragonal phase) and (g) at 763 K (cubic phase).

distortions in φ_i are not considered, since the explicit SPM expressions (eqn (S1)–(S3) in the ESI†), indicate that the changes in φ_i do not affect the axial ZFSPs. However, our calculations reveal that it is impossible to achieve any reasonable matching of the SPM predicted ZFSPs and the experimental ones for any of the three (O_{v1}^{up}, O_{v1}^{down}, O_{v2}) O-vacancy cases considered.

5.3.2. Structural model assuming Gd ions at Pb-sites. Our initial SPM calculations for the Gd^{3+} center at the Pb site in $PbTiO_3$ using the structural parameters of the host given in Table S2 in the ESI† yielded the ZFSPs as (in 10^{-4} cm^{-1}) b_2^0 = 1970.66, b_4^0 = −9.24, b_4^4 = −15.81, b_6^0 = −0.0981, and b_6^4 = 9.66. Table 9 presents the SPM/ZFSPs calculated for temperature between 10 and 765 K as well as the change of the local structural parameters R_i and θ_i of the O-ligands surrounding the Gd^{3+} center at the Pb site. The results reveal that the signs of the fourth-rank ZFSPs b_4^0 and b_4^4 are negative, which is in agreement with the low temperature data in $SrTiO_3$ (see Table 7), and do not change with temperature. The decreasing trend of b_2^0 from low to high temperature is shown in Fig. 4a, which occurs more profoundly between RT and 765 K. b_4^0 is almost constant with a slight decrease with the increase of temperature from 10 K to 765 K, whereas b_4^4 increases about two times (Fig. 4b). Compared to the fourth-rank ZFSPs, the sixth-rank ZFSPs b_6^0 and b_6^4 are much smaller, as in similar Gd^{3+} doped crystals listed in Table 7, thus obeying the expected trend $b_2^q > b_4^q > b_6^q$. The parameter b_6^0 changes sign around 520 K and becomes positive increasing by two times with temperature increasing up to 765 K, while b_6^4 remains negative and steadily decreases from -2.03×10^{-4} cm^{-1} to -1.08×10^{-4} cm^{-1} (Fig. 4c).

The temperature dependence of the O-ligand angles (θ_i) from the tetragonal C_4-axis and the O-ligand lengths (R) of the Pb^{2+} site upon Gd^{3+} substitution is shown in Fig. 4d and 4e, respectively. The ligand-lengths (R_1, R_2, R_3) alter in a different manner as follows: very slight increase in R_1 ($\Delta R_1 \approx 0.07$ Å) relative to others but a quite large increase in R_2 ($\Delta R_2 \approx 0.31$ Å), and a profound decrease in R_3 ($\Delta R_3 \approx -0.45$ Å).

Contrary to the finding reported[5] that b_4^4 for Gd^{3+} in $PbTiO_3$ showed no effect on the spectral shape within the limits of the observed linewidths, our calculations show that ZFSP b_4^4 is not only as significant as b_4^0 but also clearly changes with temperature, unlike b_4^0. The change of the configuration of the cluster $[Gd–O1_2]^{21-}$ with temperature from tetragonal phase (Fig. 4f) to cubic phase (Fig. 4g) is depicted in Fig. 4. Depending on this phase transition, the values of R_i and θ_i for the O-ligands around the Gd^{3+} center change accordingly from tetragonal to cubic ones: $\theta_1 = 90^\circ$, $\theta_2 = 135^\circ$, and $\theta_3 = 45^\circ$, whereas $R_1 = R_2 = R_3 \approx 2.8$ Å.

5.3.3. Structural model assuming the presence of oxygen vacancies around Pb-sites. Any possible O-vacancies may form from one of the oxygen ligands around the Pb site: O1, O2, or O3. Thus, we may consider three different O-vacancy cases denoted as O_{v1}, O_{v2}, and O_{v3}. Using the data extracted from the optimized structures (Table S3 in the ESI†), the ZFSPs are obtained for each case as (in 10^{-4} cm^{-1}): (i) b_2^0 = 237.43, b_4^0 = −10.75, b_4^4 = −1.19, b_6^0 = −0.045, and b_6^4 = −2.34 for O_{v1}, (ii) b_2^0 = 1121.04, b_4^0 = −5.72, b_4^4 = −36.87, b_6^0 = −0.023, and $b_6^4 = -1.91 \times 10^{-4}$ cm^{-1} for O_{v2}, and (iii) = 1363.14, b_4^0 = −8.55, b_4^4 = −23.88, b_6^0 = −0.041, and $b_6^4 = -2.41 \times 10^{-4}$ for O_{v3}. Our subsequent calculations, including these O-vacancies, reveal that we can achieve a reasonable matching for only O_{v1}. Thus, we can conclude that only the oxygen vacancy in the *ab*-plane (O1) is plausible when the dopant Gd^{3+} ion locates at the Pb-site substitutionally. The presence of an O-vacancy in the structure around the Gd^{3+} center in the Pb site results in profound local structural changes. As shown in Fig. S3 in the ESI,† this shifted the Gd^{3+} ion along the diagonal [−110]. The results of the SPM/ZFSP calculations, including local distortion parameters and their temperature dependence, are listed in Table 10 for O_{v1}. The variation of the parameters b_4^q and b_6^q with temperature in the range of 10–765 K is shown in Fig. 5. It is seen that although both b_4^0 and b_4^4 retain negative sign, b_4^0 remains almost unchanged but b_4^4 increases about three times with increasing temperature. This trend of b_4^q is similar to that obtained in the SPM analysis for the Pb-site considered above. Similar trends of

Table 10 The variation of ZFSPs and local distortion parameters with temperature calculated using SPM for the Gd^{3+} center at the Pb site with an O1-vacancy (O_{v1}); b_k^q are in (10^{-4} cm^{-1}), R_i are in (Å), and θ_i are in (°)

T (K)	b_2^0	b_4^0	b_4^4	b_6^0	b_6^4	R_1	R_2	R_3	θ_1	θ_2	θ_3
10	861.1	−9.63	−6.94	−0.027	−1.63	2.7581	2.5412	3.3281	83.72	126.76	40.34
30	855.3	−9.63	−7.04	−0.027	−1.63	2.7581	2.5414	3.3277	83.74	126.79	40.35
80	849.0	−9.64	−7.14	−0.026	−1.63	2.7582	2.5417	3.3271	83.76	126.82	40.37
120	836.7	−9.65	−7.34	−0.026	−1.63	2.7583	2.5422	3.3261	83.81	126.88	40.39
160	827.8	−9.65	−7.48	−0.025	−1.63	2.7584	2.5428	3.3249	83.84	126.93	40.41
200	812.6	−9.66	−7.69	−0.024	−1.63	2.7587	2.5433	3.3237	83.89	127.00	40.44
260	807.9	−9.66	−7.76	−0.024	−1.62	2.7589	2.5441	3.3222	83.90	127.02	40.45
293	806.8	−9.66	−7.77	−0.024	−1.62	2.7589	2.5442	3.3219	83.91	127.02	40.45
300	804.9	−9.67	−7.78	−0.024	−1.62	2.7590	2.5441	3.3217	83.91	127.03	40.45
425	735.8	−9.75	−8.72	−0.020	−1.62	2.7594	2.5452	3.3147	84.18	127.39	40.62
520	660.7	−9.79	−9.90	−0.015	−1.61	2.7601	2.5492	3.3062	84.47	127.77	40.80
620	468.5	−9.83	−12.80	−0.002	−1.55	2.7625	2.5618	3.2807	85.19	128.74	41.22
685	363.3	−9.81	−14.26	0.003	−1.52	2.7637	2.5681	3.2679	85.55	129.23	41.33
720	273.4	−9.80	−15.47	0.008	−1.48	2.7649	2.5744	3.2551	85.86	129.64	41.40
752	30.9	−9.64	−18.44	0.020	−1.40	2.7687	2.5927	3.2167	86.66	130.70	41.54
∼765	0	−10.13	−20.85	0.045	−1.00	2.807	2.807	2.807	90	135	45

b_6^q parameters are also observed using the Pb-site model and the O_{v1} one. For the latter one, b_6^0 changes sign at a higher temperature between 620 K and 685 K. As for the Pb-site model, the b_6^q values are quite comparable with the literature ones listed in Table 7.

Moreover, the changes of the local structural parameters R_i and θ_i show nearly the same trend with small variation: R_1 and R_2 increase by $\Delta R_1 \approx 0.04$ Å and $\Delta R_2 \approx 0.26$ Å, respectively, but R_3 decreases by $\Delta R_3 \approx 0.52$ Å, whereas all θ_i increase to their cubic values by $\Delta\theta_1 \approx 6.3^\circ$, $\Delta\theta_2 \approx 8.2^\circ$, and $\Delta\theta_3 \approx 4.7^\circ$ with increasing temperature. Fig. 5 shows the temperature dependencies of R_i and θ_i and the configuration of the $[Pb{-}O_{122}]^{22-}$ cluster after Gd^{3+} substitution for the Pb-site ($[Gd{-}O1_1]^{19-}$ cluster) with an O-vacancy (V_O) at low temperatures (tetragonal phase) and at 763 K (cubic phase).

Our modeling of changes of the distortion parameters with temperature for this Gd^{3+} center with a nearby O-vacancy yields quite comparable results to those obtained assuming no vacancies in the SPM analysis for the Pb-site considered above. This analysis reveals a profound temperature dependence of

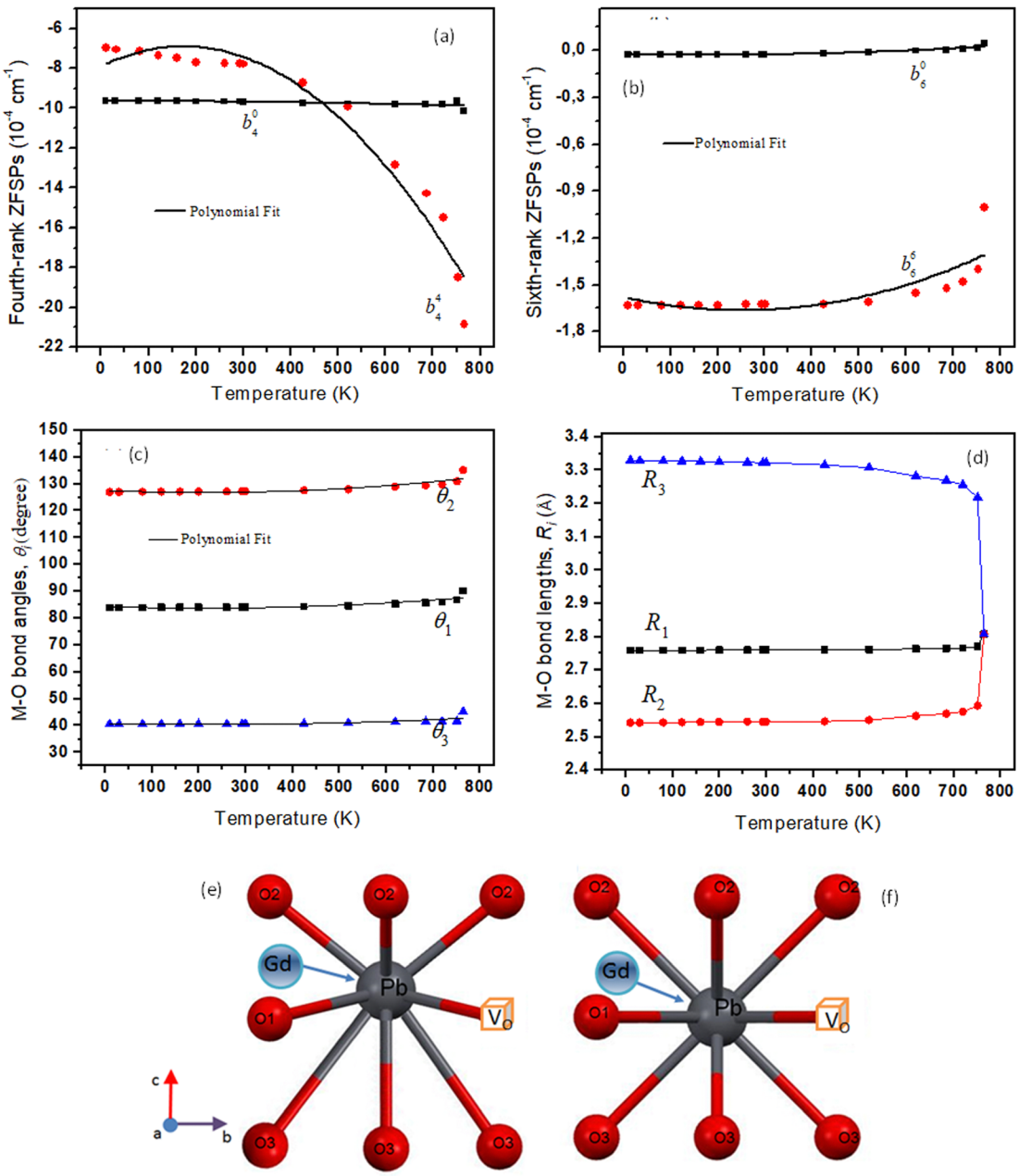

Fig. 5 The variation of ZFSPs: (a) fourth-rank and (b) sixth-rank with temperature in the range of 10–765 K in the presence of an oxygen vacancy. The polynomial curve that fits best the data of each parameter is indicated by a continuous line. Temperature dependence determined from SPM of (c) the M–O bond angles (θ) from the tetragonal C_4-axis and (d) the M–O bond lengths (R) of the Pb^{2+} site after Gd^{3+} substitution when an oxygen vacancy is present. Configuration of the $[Gd{-}O1_1]^{19-}$ cluster: (e) at low temperatures (tetragonal phase) and (f) at 763 K (cubic phase).

structural parameters especially from RT to high temperature, which is reflected in the strong temperature dependence of the ZFSP b_2^0 as well as the lattice parameter ratio c/a. This finding is corroborated by EMR[5,6] and XRD[50] measurements.

6. Summary and conclusions

The major aims of this study may be summarized as follows. First, we aimed at explaining the mechanism of structural changes occurring during the structural phase transitions in the $PbTiO_3$ crystal. Second, we aimed at providing insight into variations of spectroscopic and magnetic properties with temperature for Gd^{3+}:$PbTiO_3$ bulk and nanopowder samples with varying compositions: $Pb_{1-x}Gd_xTiO_{3-\delta}$ and $PbTi_{1-x}Gd_xTiO_{3-\delta}$, where the stoichiometric parameter δ denotes the presence of the O-vacancy.

To achieve these aims, we employed a two-fold modeling approach. First, the density functional theory (DFT) *ab initio* computations were performed using the WIEN2k code to obtain geometry optimized structural data for pure $PbTiO_3$ as well as doped systems. Using the optimized structures, we computed the formation energies of the doped compositions with and without oxygen vacancy. Provided that the electron charge densities converged through several self-consistent-field DFT computations, the results were used as input to the quantum theory of atoms in molecules (QTAIM) implemented in the CRITIC2 code. By analyzing the so-computed Bader electron charges (BECs), we qualitatively assessed the chemical stability of the pure compound and the doped compositions including and excluding the O-vacancy. We achieved consistent findings on the chemical stability and plausible site for doping Gd based on two different approaches, *i.e.*, (i) formation energy (Section 4.3) and (ii) analysis of Bader charges (Section 4.5). As discussed below these findings are further corroborated by semiempirical modeling.

Next, the computed data as well as the non-optimized XRD structural data were utilized as input for the semiempirical superposition model (SPM) analysis to investigate variations of the zero-field splitting (ZFS) parameters (ZFSPs) of Gd^{3+} doped into $PbTiO_3$ over a wide range from 5 to 780 K as well as for various compositions. The two-fold modeling approach has enabled considering possible distortions around Gd^{3+} centers and explaining the temperature dependence of ZFSPs observed in Gd^{3+}-doped $PbTiO_3$ structures, and thus correlating XRD structural data with spectroscopic EMR data.

The ZFSPs modelled using SPM were fine-tuned by matching with available experimental EMR data for Gd^{3+} probes in bulk $PbTiO_3$ and $PbTiO_3$ nanoparticles. Several possible structural models, including models taking into account the role of an O-vacancy around Gd^{3+} centers, have been considered. Variations of all ZFSPs with temperature, including the sixth-rank ones, in the range 5 to 780 K were determined for each of the structural models of Gd^{3+} centers considered. The results of SPM/ZFSP modeling utilizing the geometry optimized data obtained from DFT/*ab initio* computations allow the following conclusions to be drawn. These results strongly suggest that the Ti-site is not favorable for being replaced by Gd^{3+} neither with nor without O-vacancy in the vicinity. On the other hand, both models, *i.e.*, with/without O-vacancy, provide evidence for the plausibility of the Pb^{2+} site for Gd^{3+} dopant ions. The SPM results reveal that the structural distortions due to the bond lengths are more profound than those due to the bond angles, especially, in the range from RT (tetragonal phase) to high temperature (cubic phase).

The results of DFT/*ab initio* computations of the formation energies allow the following conclusions to be drawn. An important finding is that the formation energies calculated using the PBE-GGA functional for $Pb_{0.875}Gd_{0.125}TiO_3$, $PbTi_{0.875}Gd_{0.125}O_3$, $Pb_{0.875}Gd_{0.125}TiO_{3-\delta}$, and $PbTi_{0.875}Gd_{0.125}O_{3-\delta}$ compounds reveal that the Pb-site is more favorable than the Ti-site for Gd^{3+} dopant ions in the absence of the O-vacancy. Hence, the SPM analysis of ZFSPs together with the EMR results over a wide range of temperature, in agreement with the *ab initio* prediction deduced from the formation energies, provides evidence that the Pb^{2+} site is more plausible as the Gd^{3+} substitution site. This is quite an important result for the rare-earth metal ions, since it differs from that expected for transition-metal ions. Moreover, it is in agreement with the experimental findings that the Gd^{3+} substitution occurs at Pb^{2+} site with the formation of lead vacancies in distant coordination spheres.

The overall conclusions are as follows. The present results amply show the usefulness of the two-fold modeling approach for comprehensive analysis of the structural changes occurring around Gd^{3+}:$PbTiO_3$ and their effects on the spectroscopic and magnetic properties. This approach enables more reliable assessment of various structural models, and thus better correlation between structural data and the spectroscopic and magnetic properties observed for Gd^{3+}:$PbTiO_3$ bulk and nanopowder samples with varying compositions. The SPM-calculated ZFSPs enable better interpretation of the available experimental EMR data. Importantly, the modeling approach utilized in this study may also be useful in future studies aimed at technological applications of the $PbTiO_3$ host as well as other materials doped with various RE and TM ions.

Conflicts of interest

There are no conflicts to declare.

Acknowledgements

This work was partially supported by the research grant # UMO-2016/21/B/ST4/02064 from the Polish National Science Center. The DFT/*ab initio* computations were carried out at the Poznan Supercomputing and Networking Center. This work, as a part of the postdoctoral project of Leila Mollabashi, is supported by the University of Isfahan (UI) with the number 150/1400 and dated 1400/08/15. We thank Dr Tomasz Ślusarski for guidance on computational aspects at the early stages of this work and

Farhad Jalali-Asadabadi for his friendly contribution and nice graphical assistance.

References

1 R. E. Cohen, *Nature*, 1992, **358**, 136–138.
2 L. Bellaiche and D. Vanderbilt, *Phys. Rev. B: Condens. Matter Mater. Phys.*, 2000, **61**, 7877–7882.
3 Z. Zhang, J. Xu, L. Yang, S. Liu, J. Xiao, R. Zhu, X. Li, X. Wang and H. Luo, *J. Appl. Phys.*, 2019, **125**, 034104.
4 R. A. Eichel, *J. Electroceram.*, 2007, **19**, 9–21.
5 R. A. Eichel, H. Meštri, H. Kungl and M. J. Hoffmann, *Appl. Phys. Lett.*, 2006, **88**, 122506.
6 J. van Tol, K. P. Dinse, H. Kungl and M. J. Hoffmann, *Appl. Magn. Reson.*, 2009, **36**, 297–307.
7 E. Erdem, P. Jakes, S. K. S. Parashar, K. Kiraz, M. Somer, A. Rüdiger and R.-A. Eichel, *J. Phys.: Condens. Matter*, 2010, **22**, 345901.
8 C. Rudowicz, *Magn. Reson. Rev.*, 1987, **13**, 1–89. Erratum: C. Rudowicz, Magn. Res. Rev., 1987, 13, 335.
9 C. Rudowicz and S. K. Misra, *Appl. Spectrosc. Rev.*, 2001, **36**, 11–63.
10 C. Rudowicz and M. Karbowiak, *Coord. Chem. Rev.*, 2015, **287**, 28–63.
11 P. Hohenberg and W. Kohn, *Phys. Rev.*, 1964, **136**, B864–B871.
12 W. Kohn and L. J. Sham, *Phys. Rev.*, 1965, **140**, A1133–A1138.
13 P. Blaha, K. Schwarz, G. K. H. Madsen, D. Kvasnicka, J. Luitz, R. Laskowski, F. Tran and L. D. Marks, *WIEN2k_22.1: An Augmented Plane Wave plus Local Orbitals Program for Calculating Crystal Properties*, Vienna University of Technology, Austria, 2022, **https://wien2k.at/reg_user/textbooks/usersguide.pdf**.
14 P. Blaha, K. Schwarz, F. Tran, R. Laskowski, G. K. H. Madsen and L. D. Marks, *J. Chem. Phys.*, 2020, **152**, 074101.
15 R. F. W. Bader, *Chem. Rev.*, 1991, **91**, 893.
16 R. F. W. Bader, *Atoms in Molecules: A Quantum Theory (International Series of Monographs on Chemistry)*, Oxford University Press, 1994.
17 A. O. de-la Roza, M. Blanco, A. M. Pendás and V. Luaña, *Computer Phys. Commun.*, 2009, **180**, 157.
18 A. O. de-la Roza, E. R. Johnson and V. Luaña, *Computer Phys. Commun.*, 2014, **185**, 1007.
19 D. J. Newman and W. Urban, *Adv. Phys.*, 1975, **24**, 793–844.
20 M. Andrut, M. Wildner and C. Rudowicz, Optical absorption spectroscopy in geosciences. Part II, Quantitative aspects of crystal fields, in *Spectroscopic Methods in Mineralogy-European Mineralogical Union Notes in Mineralogy*, ed. A. Beran and E. Libowitzky, Eötvös University Press, Budapest, 2004, vol. 6, ch. 4, p. 145.
21 C. Rudowicz, P. Gnutek and M. Açikgöz, *Appl. Spectrosc. Rev.*, 2019, **54**(8), 673–718.
22 A. Gorczyński, D. Marcinkowski, M. Kubicki, M. Löffler, M. Korabik, M. Karbowiak, P. Wiśniewski, V. Patroniak and C. Rudowicz, *Inorg. Chem. Front.*, 2018, **5**, 605–618.
23 D. Marcinkowski, A. Adamski, M. Kubicki, G. Consiglio, V. Patroniak, T. Ślusarski, M. Açıkgöz, D. Szeliga, N. Vadra, M. Karbowiak, I. Stefaniuk, C. Rudowicz, A. Gorczyński and M. Korabik, *Dalton Trans.*, 2022, **51**, 12041–12055.
24 G. Aromí and E. K. Brechin, *Struct. Bonding*, 2006, **122**, 1–67.
25 C. Coulon, H. Misayaka and R. Clérac, *Struct. Bonding*, 2006, **122**, 163–206.
26 H. L. C. Feltham and S. Brooker, *Coord. Chem. Rev.*, 2014, **276**, 1–33.
27 J. Tang and P. Zhang, *Lanthanide Single Molecular Magnets*, Springer-Verlag, Berlin, Heidelberg, 2015.
28 S. K. Singh, M. F. Beg and G. Rajaraman, *Chem. – Eur. J.*, 2016, **22**, 672–680.
29 N. F. Chilton, S. K. Langley, B. Moubaraki, A. Soncini, S. R. Batten and K. S. Murray, *Chem. Sci.*, 2013, **4**, 1719–1730.
30 S. Demir, M. Nippe, M. I. Gonzalez and J. R. Long, *Chem. Sci.*, 2014, **5**, 4701–4711.
31 S. Goswami, A. Adhikary, H. S. Jena and S. Konar, *Dalton Trans.*, 2013, **42**, 9813–9817.
32 P. I. Girginova, L. C. J. Pereira, J. T. Coutinho, I. C. Santos and M. Almeida, *Dalton Trans.*, 2014, **43**, 1897.
33 M. Fik-Jaskółka, A. Gorczyński, D. Marcinkowski, M. Kubicki, V. Patroniak, I. Stefaniuk, M. Wencka, T. Ślusarski, M. Açıkgöz, D. Piwowarska, P. Gnutek, M. Korabik, M. Karbowiak and C. Rudowicz, Low and high symmetry aspects at the interface between the semiempirical and ab initio modelling of ZFS parameters and EMR spectroscopy – study case: trigonal and triclinic binuclear GdIII complexes, revised version submitted on 23.12.22 to Dalton Transactions, under review.
34 G. Franco-Rivera, J. Cochran, L. Chen, S. Bertaina and I. Chiorescu, *Phys. Rev. Appl.*, 2022, **18**, 014054.
35 J. A. Weil and J. R. Bolton, *Electron Paramagnetic Resonance, Elemental Theory and Practical Applications*, Wiley, New York, 2007.
36 F. E. Mabbs and D. Collison, *Electron Paramagnetic Resonance of d Transition-Metal Compounds*, Elsevier, Amsterdam, 1992.
37 *Multifrequency Electron Paramagnetic Resonance*, ed. S. K. Misra, Wiley-VCH, Weinheim, 2011, S.K. Misra, C. Rudowicz, Erratum, **https://www.wiley-vch.de/publish/dt/books/ISBN3-527-40779-0**.
38 J. R. Pilbrow, *Transition-Ion Electron Paramagnetic Resonance*, Clarendon Press, Oxford, 1992.
39 R. Boča, *Coord. Chem. Rev.*, 2004, **248**, 757–815.
40 R. Boča, *Struct. Bond.*, 2006, **117**, 1–264.
41 C. Rudowicz, *J. Phys. C: Solid State Phys.*, 1985, **18**, 1415–3015; Erratum: ibidem 1985, **18**, 3837.
42 C. Rudowicz and C. Y. Chung, *J. Phys.: Cond. Matter.*, 2000, **16**, 5825–5847.
43 C. Rudowicz and J. Qin, *J. Lumin.*, 2004, **110**, 39–64.

44 A. M. Glazer and S. A. Mabud, *Acta Crystallogr.*, 1978, **34**, 1065–1070.
45 G. Shirane, S. Hoshino and K. Suzuki, *Phys. Rev.*, 1950, **80**, 1105–1106.
46 H. Morioka, T. Yamada, A. K. Tagantsev, R. Ikariyama, T. Nagasaki, T. Kurosawa and H. Funakubo, *Appl. Phys. Lett.*, 2015, **106**, 042905.
47 J. Kobayashi, Y. Uesu, Y. Sakami and T. Hosokawa, *Ferroelectrics*, 1981, **37**, 571–574.
48 E. Erdem and R. Eichel, Impact of Defect Structure on 'Bulk' and Nano-Scale Ferroelectrics, in *Ferroelectrics-Characterization and Modeling*, ed. M. Lallart, IntechOpen, London, 2011, DOI: 10.5772/18868.
49 R. A. Eichel, *Phys. Chem. Chem. Phys.*, 2011, **13**, 368–384.
50 P. S. Dobal, R. R. Das, B. Roy, R. S. Katiyar, S. Jain and D. C. Agrawal, *J. Raman Spectrosc.*, 2000, **31**, 965–970.
51 A. P. Barranco, Y. M. Gonzalez, D. C. Arnold, D. J. Keeble and P. S. Gregoire, *J. Mater. Sci.*, 2012, **47**, 1094–1099.
52 A. Peláiz-Barranco, J. D. S. Guerra, F. Calderón-Piñar, C. Aragó, O. García-Zaldívar, R. López-Noda, J. A. Gonzalo and J. A. Eiras, *J. Mater. Sci.*, 2009, **44**, 204.
53 M. Yazdani-Kachoei, S. Rahimi, R. Ebrahimi-Jaberi, J. Nematollahi and S. Jalali-Asadabadi, *Sci. Rep.*, 2022, **12**, 663.
54 M. Yazdani-Kachoei and S. Jalali-Asadabadi, *RSC Adv.*, 2019, **9**, 36182.
55 E. Sjöstedt, L. Nordström and D. Singh, *Solid State Commun.*, 2000, **114**, 15–20.
56 G. K. H. Madsen, P. Blaha, K. Schwarz, E. Sjöstedt and L. Nordström, *Phys. Rev. B: Condens. Matter Mater. Phys.*, 2001, **64**, 195134.
57 A. D. Becke, *J. Chem. Phys.*, 1993, **98**, 1372–1377.
58 M. Shafiq, I. Ahmad and S. Jalali-Asadabadi, *RSC Adv.*, 2015, **5**, 31496.
59 M. Shafiq, I. Ahmad and S. Jalali Asadabadi, *J. Appl. Phys.*, 2014, **116**, 103905.
60 M. Zarshenas and S. Jalali Asadabadi, *Thin Solid Films*, 2012, **520**, 2901–2908.
61 P. Novák, J. Kuneš, L. Chaput and W. E. Pickett, *Phys. Status Solidi B*, 2006, **243**, 559.
62 L. Bjaalie, A. Verma, B. Himmetoglu, A. Janotti, S. Raghavan, V. Protasenko, E. H. Steenbergen, D. Jena, S. Stemmer and C. G. Van de Walle, *Phys. Rev. B: Condens. Matter Mater. Phys.*, 2015, **92**, 085111.
63 J. P. Desclaux, *Comput. Phys. Commun.*, 1975, **9**, 31–45.
64 D. J. Singh and L. Nordstrom, *Planewaves, Pseudopotentials, and the Linearized APW (LAPW) method*, Springer Science & Business Media, 2006.
65 M. Rafiee and S. Jalali Asadabadi, *Comput. Mater. Sci.*, 2009, **47**, 584.
66 H. J. Monkhorst and J. D. Pack, *Phys. Rev. B: Solid State*, 1976, **13**, 5188–5192.
67 D. A. Carballo-Córdova, *Philos. Mag.*, 2019, **99**, 181–197.
68 M. Yazdani-Kachoei, S. Jalali-Asadabadi and N. Arianmehr, *Comput. Mater. Sci.*, 2019, **164**, 205–217.
69 F. Birch, Finite elastic strain of cubic crystals, *Phys. Rev.*, 1947, **71**, 809–824.
70 S. F. Yuk, K. C. Pitike, S. M. Nakhmanson, M. Eisenbach, Y. W. Li and V. R. Cooper, *Sci. Rep.*, 2017, **7**, 1–10.
71 R. Nishino, T. C. Fujita, F. Kagawa and M. Kawasaki, *Sci. Rep.*, 2020, **10**, 1–8.
72 S. Rahimi, R. Ebrahimi-Jaberi, F. Jalali-Asadabadi, L. Mollabashi and S. Jalali-Asadabadi, *Phys. Rev. B*, 2022, **106**, 115205.
73 V. Bhide, K. Deshmukh and M. Hegde, *Physica*, 1962, **28**, 871–876.
74 U. V. Waghmare and K. M. Rabe, *Phys. Rev. B: Condens. Matter Mater. Phys.*, 1997, **55**, 6161–6173.
75 Y. Wang, H. Zhao, L. Zhang, J. Chen and X. Xing, *Phys. Chem. Chem. Phys.*, 2017, **19**, 17493–17515.
76 T. Shimada, T. Xu, Y. Araki, J. Wang and T. Kitamura, *Nano Lett.*, 2017, **17**, 2674–2680.
77 P. Ghosez and K. Rabe, *Appl. Phys. Lett.*, 2000, **76**, 2767–2769.
78 Y. Xiao and K. Bhattacharya, Smart Structures and Materials: Active Materials: Behavior and Mechanics, *Proc. SPIE*, 2004, **5387**, 354–365.
79 T. Shimada, Y. Uratani and T. Kitamura, *Appl. Phys. Lett.*, 2012, **100**, 162901.
80 X. Wang, T. Xu, F. Xuan, C. Chen, T. Shimada and T. Kitamura, *J. Appl. Phys.*, 2019, **126**, 174107.
81 F. Miao, S.-J. Liang and B. Cheng, *npj Quantum Mater.*, 2021, (6), 1–4.
82 J. A. Brehm, H. Takenaka, C. W. Lee, I. Grinberg, J. W. Bennett, M. R. Schoenberg and A. M. Rappe, *Phys. Rev. B: Condens. Matter Mater. Phys.*, 2014, **89**, 195202.
83 A. J. Kalinichev, J. D. Bass, B. N. Sun and D. A. Payne, *J. Mater. Res.*, 1997, **12**(10), 2623–2627.
84 M. Yazdani-Kachoei and S. Jalali-Asadabadi, *J. Alloys Compd.*, 2020, **828**, 154287.
85 J. M. Skelton, D. Tiana, S. C. Parker, A. Togo, I. Tanaka and A. Walsh, *J. Chem. Phys.*, 2015, **143**, 064710–064715.
86 L. Mollabashi and S. Jalali-Asadabadi, *Phys. Rev. B: Condens. Matter Mater. Phys.*, 2020, **102**, 045120.
87 M. Yazdani-Kachoei, S. Jalali-Asadabadi, I. Ahmad and K. Zarringhalam, *Sci. Rep.*, 2016, **6**, 1–17.
88 L. Zhang, I. Bredeson, A. Y. Birenbaum, P. R. C. Kent and V. R. Cooper, *Phys. Rev. Mater.*, 2018, **2**(6), 064409.
89 A. Emery and C. Wolverton, *Sci. Data*, 2017, **4**, 170153.
90 P. Erhart and K. Albe, *J. Appl. Phys. Rev.*, 2007, **102**, 084111.
91 J. P. Desclaux and Y.-K. Kim, *J. Phys. B: At. Mol. Phys.*, 1975, **8**, 1177.
92 S. Jalali-Asadabadi, S. Cottenier, H. Akbarzadeh, R. Saki and M. Rots, *Phys. Rev. B: Condens. Matter Mater. Phys.*, 2002, **66**, 195103.
93 S. Jalali-Asadabadi and H. Akbarzadeh, *Physica B: Cond. Mat.*, 2004, **349**, 76.
94 S. Jalali-Asadabadi, *Phys. Rev. B: Condens. Matter Mater. Phys.*, 2007, **75**, 205130.
95 P. Perdew, K. Burke and M. Ernzerhof, *Phys. Rev. Lett.*, 1996, **77**, 3865.
96 F. Wang, Y. Xie, J. Chen, H. Fu and X. Xing, *Phys. Chem. Chem. Phys.*, 2014, **16**, 5237.

97 P. Perdew, K. Burke and M. Ernzerhof, *Phys. Rev. Lett.*, 1996, **77**, 3865.
98 G. Kresse and J. Furthmuller, *Phys. Rev. B: Condens. Matter Mater. Phys.*, 1996, **54**, 11169–11186.
99 M. Pavone, A. M. Ritzmann and E. A. Carter, *Energy Environ. Sci.*, 2011, **4**, 4933.
100 P. Pitriana, T. D. K. Wungu, H. Herman and R. Hidayat, *Results Phys.*, 2019, **15**, 102592.
101 S. Pöykkö and D. Chadi, *J. Phys. Chem. Solids*, 2000, **61**, 291.
102 M. Açıkgöz and P. Gnutek, *Opt. Mater.*, 2014, **36**, 1311–1318.
103 M. Açıkgöz, P. Gnutek and C. Rudowicz, *Opt. Mater.*, 2014, **36**, 1342–1349.
104 C. Rudowicz, P. Gnutek and M. Açıkgöz, *Opt. Mater.*, 2015, **46**, 254–259.
105 C. Rudowicz, *J. Phys. C: Solid State Phys.*, 1987, **20**, 6033–6037.
106 P. Gnutek P, M. Açıkgöz and C. Rudowicz, *Opt. Mater.*, 2010, **32**, 1161–1169.
107 M. Açıkgöz M, P. Gnutek and C. Rudowicz, *Solid State Commun.*, 2010, **150**, 1077–1081.
108 W. C. Zheng and S. Y. Wu, *Physica B*, 2001, **304**, 137–140.
109 S.-Y. Wu and H.-N. Dong, *Supercond. Sci. Technol.*, 2005, **18**, 611–614.
110 Vishwamittar and S. P. Puri, *J. Chem. Phys.*, 1974, **61**, 3720–3727.
111 S.-Y. Wu and H.-N. Dong, *Physica C*, 2005, **424**, 40–44.
112 S. K. Misra and X. Li, *J. Phys.: Cond. Matter*, 1990, **2**, 9613–9620.
113 S. K. Misra, X. Li, L. E. Misiak and C. Wang, *Physica B: Cond. Mat.*, 1990, **167**, 209–219.
114 F. Prissok and G. Lehmann, *J. Phys.: Cond. Matter*, 1990, **1**, 5381–5488.
115 S. Y. Wu, H. N. Dong, J. Z. Lin and Q. Fu, *Radiat. Eff. Defects Solids*, 2006, **161**, 505–510.
116 J. A. Aramburu, P. García-Fernandez, M. T. Barriuso and M. Moreno, *J. Phys. Chem. A*, 2013, **117**, 12642–12647.
117 A. Rothschild, W. Menesklou, H. L. Tuller and E. Ivers-Tiffee, *Chem. Mater.*, 2006, **18**, 3651–3659.
118 W.-Q. Yang and W. C. Zheng, *Spectrochim. Acta, Part A*, 2011, **79**, 1291–1294.
119 W.-Q. Yang, Y. Lin, W. Huang and H.-Z. Zeng, *Physica B*, 2012, **407**, 1268–1271.
120 W.-Q. Yang, W. C. Zheng and H.-G. Liu, *Physica B*, 2011, **406**, 3450–3453.
121 L. Rimai and G. A. de Mars, *Phys. Rev.*, 1962, **127**, 702–710.
122 M. M. Abraham, G. W. Clark, C. B. Finch, R. W. Reynolds and H. Zeldes, *J. Chem. Phys.*, 1969, **50**, 2057–2062.
123 J. Rosenthal and R. F. Riley, *Phys. Rev.*, 1969, **177**, 625–628.
124 C. Linares and A. Louat, *J. Phys.*, 1975, **36**, 717–725.
125 A. Rockenbauer, A. Janossy, L. Korecz and S. Pekker, *J. Magn. Reson.*, 1967, **97**, 540.

